https://doi.org/10.5194/egusphere-2026-1745
Preprint. Discussion started: 16 April 2026

High-frequency monitoring of SO_2 plumes from moderate-scale volcanic eruptions using a synergy of GEO and LEO satellites: A case study of the 2024 Kanlaon eruption

Shangyi Liu[1], Yingjun Zheng[1], Mengya Sheng[1], Lu Lee[2], Chengli Qi[2], Feng Lu[2], Bruno Franco[3], Lieven Clarisse[3], Cathy Clerbaux[3,4], Nicolas Theys[5], Jhoon Kim[6,7], Zhao-Cheng Zeng[1,*]

[1] School of Earth and Space Sciences, Peking University, Beijing, China
[2] Innovation Center for FengYun Meteorological Satellite, Key Laboratory of Radiometric Calibration and Validation for Environmental Satellites, National Satellite Meteorological Center, China Meteorological Administration, Beijing 100081, China
[3] Université libre de Bruxelles (ULB), BLU-ULB research Center, Spectroscopy, Quantum Chemistry and Atmospheric Remote Sensing (SQUARES), Brussels, Belgium
[4] LATMOS/IPSL, Sorbonne Université, UVSQ, CNRS, Paris, France
[5] Royal Belgian Institute for Space Aeronomy (BIRA-IASB), Brussels, Belgium
[6] Department of Atmospheric Science, Yonsei University, Seoul, Korea
[7] Max Planck Institute for Meteorology, Hamburg, Germany

Correspondence to: Zhao-Cheng Zeng (zczeng@pku.edu.cn)

Abstract. Satellite remote sensing is crucial for monitoring volcanic sulfur dioxide (SO_2) globally. However, the rapid evolution of volcanic plumes necessitates high-frequency observations, which typical twice-daily overpasses of Low Earth Orbit (LEO) sensors fail to capture. To address this limitation, this study presents a synergistic Geostationary Earth Orbit (GEO) and LEO observation framework. Specifically, we show the first quantitative SO_2 retrieval from a GEO hyperspectral infrared sounder (FY-4B/GIIRS), using an optimal-estimation-based retrieval algorithm. Because current and upcoming GEO infrared sounders lack the strong $\nu 3$ absorption band, our algorithm uniquely leverages the weaker $\nu 1$ absorption band. Simulation experiments indicate that the detection limit (retrieval error > 100%) is 3 DU for plumes at 10 km altitude. During the June 2024 Kanlaon eruption, GIIRS captured early, high-concentration plume dynamics, though tracking diluted plumes remained challenging. Crucially, it provided the earliest satellite detection by continuously monitoring the initial nighttime burst (posterior error of 53.7 ± 24.1%), filling critical temporal gaps left by ultraviolet sensors. Combined with LEO (HIRAS, IASI, CrIS, TROPOMI and MLS) and GEO sensor (GEMS), the synergistic framework achieved high frequency quantification of SO_2 mass loading and transport pathways. We estimated a peak SO_2 mass loading of ~40 kt and an e-folding time of 5.2 ± 0.5 days. Furthermore, multi-platform observations identified significant discrepancies in the CAMS global model regarding the plume's evolution and magnitude. This geostationary-driven synergistic framework delivers high-fidelity observational records, establishing a robust basis for monitoring moderate-scale volcanic events and evaluating atmospheric chemical transport models.

https://doi.org/10.5194/egusphere-2026-1745
Preprint. Discussion started: 16 April 2026

1 Introduction

Volcanic eruptions inject immense quantities of gases and particulates into the atmosphere. Among these emissions, sulfur dioxide (SO_2) is of particular importance due to its profound influence on global climate, environment and human activities **(Robock, 2000; Timmreck, 2012)**. Upon injection into the upper troposphere-lower stratosphere, SO_2 oxidizes into sulfate aerosols that efficiently scatter solar radiation, altering the Earth's energy balance and atmospheric circulation **(e.g., Schmidt et al., 2018**). Its surface dispersion degrades air quality and causes acid rain, posing risks to ecosystems and public health **(e.g., Schmidt et al., 2011; Wang et al., 2016)**. Additionally, SO_2 serves as a reliable proxy for tracking co-emitted volcanic ash, which severely threatens aviation safety by reducing visibility and causing damage to aircraft engines **(e.g., Prata, 2009)**. Historically, scientific attention has mainly focused on catastrophic, large-scale explosive eruptions, such as the 1991 Pinatubo and the 2022 Hunga Tonga-Hunga Ha'apai events. However, small-to-medium scale eruptions occur with much greater frequency. Though individually minor, their cumulative emissions contribute significantly to the global sulfate aerosol background and radiative forcing **(Mills et al., 2016).** Consequently, accurately tracking and quantifying SO_2 emissions from these rapidly evolving small-scale eruptions is crucial for comprehensive climate and environmental assessments.

Satellite remote sensing serves as a unique tool for tracking volcanic SO_2 plumes, offering distinct advantages such as comprehensive global coverage, the safe monitoring of hazardous and inaccessible regions, and overall cost-effectiveness. Over the past few decades, global volcanic SO_2 monitoring has been primarily achieved by using Low Earth Orbit (LEO) sensors. These observations mainly exploit SO_2 absorption features in the ultraviolet (UV) and infrared (IR) spectral regions. The representative UV instruments include TOMS **(e.g., Krueger, 1983)**, GOME **(e.g., Eisinger & Burrows, 1998)**, SCIAMACHY **(e.g., Lee et al., 2008)**, OMI **(e.g., Krotkov et al., 2006; Theys et al., 2015)**, GOME-2 **(e.g., Rix et al., 2012)**, OMPS **(e.g., Yang et al., 2013)** and TROPOMI **(e.g., Queißer et al., 2019; Theys et al., 2017)**. In the infrared, these sounders include MODIS **(e.g., Corradini et al., 2009)**, ASTER **(e.g., Urai, 2004)**, AIRS **(e.g., Carn et al., 2005)**,TES (**e.g., Clerbaux et al., 2008**), IASI **(e.g., Carboni et al., 2012; Clarisse et al., 2008; Walker et al., 2012)**, CrIS **(Hyman & Pavolonis, 2020)**, and HIRAS **(Li et al., 2025; Zeng et al., 2025)**. Additionally, volcanic SO_2 can also be retrieved from microwave band measurements, such as MLS **(e.g., Pumphrey et al., 2015)**.

Despite their exceptional spectral resolution and sensitivity, the instruments onboard LEO platforms are constrained by relatively long revisit cycles (typically 12–24 hours). Such temporal sampling may not fully capture rapid SO_2 plume dynamics, especially from small to moderate volcanic eruptions. To improve temporal resolution, Geostationary Earth Orbit (GEO) satellites have been utilized. They provide near-continuous and higher frequency observations, compared to polar-orbiting platforms. However, conventional GEO platforms equipped with multispectral imagers, such as SEVIRI **(e.g., Prata & Kerkmann, 2007)** and GOES **(e.g., Ackerman et al., 2008)** rely on broad spectral channels. This limitation results in high detection limits and strong interference from water vapor and volcanic ash, making precise quantitative SO_2 estimation extremely difficult. For example, SEVIRI retrievals exhibit conservative single-pixel errors as high as ±10 DU. Recently, the advent of GEO UV hyperspectral sounders, such as GEMS **(Park et al., 2023)** and TEMPO **(Li et al., 2025)**, has provided

https://doi.org/10.5194/egusphere-2026-1745
Preprint. Discussion started: 16 April 2026

unprecedented hourly observations. However, UV-based retrievals are strictly limited to daytime and may suffer from biases at high observation and solar zenith angles. In essence, every single-sensor approach presents inherent limitations. Therefore, to overcome the trade-offs between temporal coverage, retrieval precision, and diurnal continuity, developing a synergistic multi-satellite observation framework is essential. By integrating different orbits and spectral ranges, such a collaborative approach effectively compensates for the limitations of single sensors especially for small-to-medium eruptions. Within this synergy, geostationary hyperspectral infrared sounders play a crucial role, as they uniquely offer the potential for high-frequency, quantitative monitoring during both day and night.

The Geostationary Interferometric Infrared Sounder (GIIRS) onboard China's Fengyun-4B (FY-4B) satellite, launched in 2021, represents the world's first operational geostationary infrared hyperspectral sounder **(Li et al., 2022a)**. Operating with a fine spectral resolution of 0.625 cm^{-1} (comparable to CrIS), FY-4B/GIIRS empowers near-continuous, day-and-night hyperspectral monitoring every two hours. Its capability to detect various trace gases, including carbon monoxide **(Zeng et al., 2023a)**, ammonia **(Zeng et al., 2023b)**, formic acid **(Zeng et al., 2024)**, and ozone **(Liu et al., 2025)**, has been well-documented. However, quantitative volcanic SO_2 monitoring using GIIRS poses a unique challenge due to its inherent spectral limitations. Unlike traditional infrared sounders that rely on the strong SO_2 $\nu 3$ absorption band (near 1362 cm^{-1}), the spectral coverage of GIIRS is restricted to only a portion of the significantly weaker $\nu 1$ band (centered at 1152 cm^{-1}). Similarly, the Infrared Sounder (IRS) onboard the geostationary European Meteosat Third Generation (MTG) satellite, launched in 2025, also lacks coverage of this strong $\nu 3$ band **(EUMETSAT, 2025)**. Consequently, determining whether this weak absorption feature can be effectively exploited to quantify rapidly evolving SO_2 plumes from small-to-medium eruptions has remained a critical research gap.

Based on the research gap, this study aims to: (1) develop a quantitative SO_2 retrieval algorithm for FY-4B/GIIRS to exploit its high-frequency and continuous monitoring potential; and (2) establish a synergistic analytical framework integrating GIIRS with multi-source satellite observations. This framework illustrates how multi-sensor synergy enhances the capability to characterize SO_2 plume dynamics and improves the accuracy of mass flux estimates. To enhance monitoring capabilities, a comprehensive high-and-low orbit synergistic framework is constructed. This system integrates multi-source data across various overpass times, including: morning (FY-3F/HIRAS, Metop-B/C IASI), afternoon (TROPOMI, JPSS-1/2 CrIS), and dawn-dusk (FY-3E/HIRAS) orbits, alongside limb-sounding (MLS) and geostationary (GIIRS and GEMS) observations. We perform cross-validation and joint analysis across the different sensors. SO_2 retrievals for the Fengyun payloads (GIIRS, HIRAS) and CrIS are processed using algorithms developed in this study, while data for TROPOMI, IASI, GEMS, and MLS are obtained from official Level-2 products. The proposed algorithm and framework are applied to the Kanlaon volcano (Philippines) eruption on June 3, 2024. This event, characterized by a moderate SO_2 load and rapid evolution, serves as an ideal case for validating the capacity of our methodology to capture small-to-medium volcanic activities.

The remainder of this paper is organized as follows. Section 2 details the satellite instruments utilized in this study. Section 3 describes the SO_2 retrieval algorithm developed specifically for GIIRS, HIRAS and CrIS. Section 4 evaluates the algorithm's performance through simulation experiment. Section 5 presents the multi-platform retrieval results, calculates the emitted SO_2

https://doi.org/10.5194/egusphere-2026-1745
Preprint. Discussion started: 16 April 2026

mass, and conducts a cross-comparison analysis. This section also discusses the discrepancies between the satellite observations and atmospheric chemical transport model simulations. Finally, Section 6 summarizes the main findings and provides an outlook for future research.

2 Satellite measurements

2.1 Synergistic Multi-Satellite Observation Framework

The synergistic GEO-LEO observation framework used in this study is shown in Fig. 1. The framework integrates two distinct observational assets: GEO satellites (GIIRS and GEMS) capture rapid dynamics during the initial eruption phase with high-frequency monitoring, while a LEO constellation (HIRAS, CrIS, IASI, TROPOMI, and MLS) provides global coverage and altitude information on SO2 plumes. The specific instrumental configurations are summarized in Table 1.

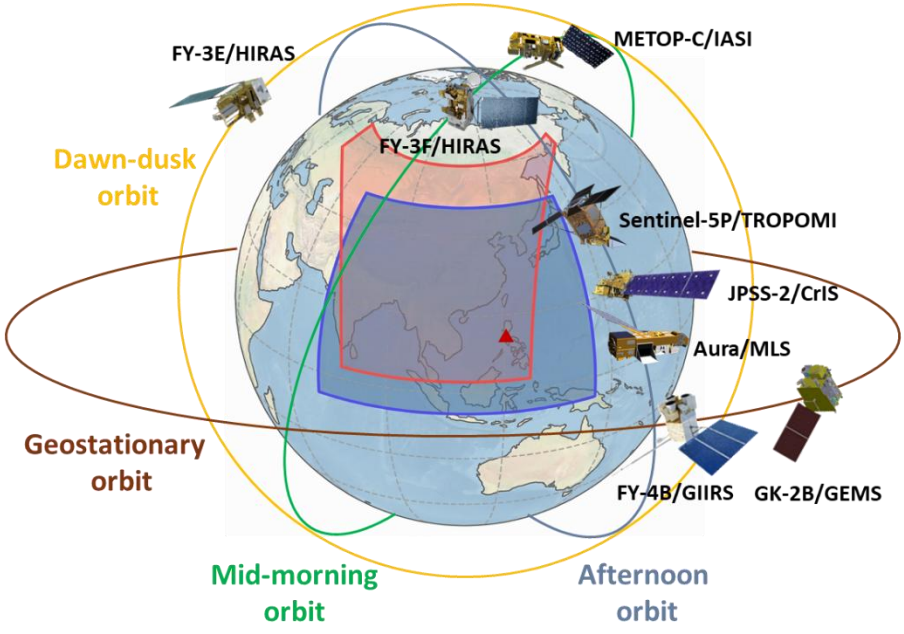

Figure 1: Schematic diagram of the synergistic GEO-LEO observation framework established for full-lifecycle volcanic SO2 monitoring. GEO: high-cadence observations for capturing rapid plume dynamics. The red and blue shaded regions represent the coverage of FY-4B/GIIRS and GEMS, respectively. LEO: global coverage measurements and vertical profiling capabilities. The constellation includes HIRAS, CrIS, IASI, TROPOMI, and MLS. The red triangle marks the location of the Kanlaon volcano (10.4°N, 123.1°E).

https://doi.org/10.5194/egusphere-2026-1745
Preprint. Discussion started: 16 April 2026

Table 1. Summary of the satellite instruments utilized in this study for volcanic SO_2 monitoring.

Sensor	Satellite platform	Footprint Size (km)	Spectral Range	Equator Crossing Time (Local)	Temporal Resolution (hour)
Geostationary (GEO) Sensors					
GIIRS	FY-4B	12	678.75–1131.25 1648.75–2251.25 cm^{-1}	\	2
GEMS	GK-2B	3.5 × 7.7	300–500 nm	\	1
Low Earth Orbit (LEO) Sensors					
HIRAS	FY-3E/F	14	658.75–2551.25 cm^{-1}	05:30 AM/PM (FY-3E) 10:00 AM/PM (FY-3F)	12
CrIS	JPSS-1/2	14	650–1095 1210–1750 2155–2550 cm^{-1}	01:30 AM/PM	12
IASI	Metop-B/C	12	645–2760 cm^{-1}	09:30 AM/PM	12
TROPOMI	Sentinel-5P	3.5 × 5.5	270–500 675–775 2305–2385 nm	01:30 PM	24
MLS	Aura	~2.7 (Vertical) ~167 (Horizontal)	118, 190, 240, 640 GHz, 2.5 THz	01:30 AM/PM	12

2.2 Geostationary Satellite Observations

2.2.1 GIIRS

GIIRS onboard the FY-4B satellite is a hyperspectral Fourier transform spectrometer. It provides full-disk scans of East Asia every two hours with a nadir spatial resolution of approximately 12 km and a spectral resolution of 0.625 cm^{-1}, enabling continuous day-and-night monitoring. As illustrated in the spectral coverage bars (Fig. 2a), the GIIRS spectral range truncates at 1131.25 cm^{-1} and does not cover the strong SO_2 $\nu 3$ absorption band (~1360 cm^{-1}), consequently this study utilizes a spectral retrieval window of 1000–1131.25 cm^{-1} which captures the available portion of the weaker $\nu 1$ absorption band for SO_2 detection. Specifically, the mean long-wave infrared spectrum observed by GIIRS over the potential plume area (0–20°N) on June 2, 2024, and its corresponding in-orbit Noise Equivalent differential Radiance (NEdR) are presented in Figs. S1(a) and S1(b), respectively. This in-orbit noise performance demonstrates high consistency with pre-launch laboratory tests, remaining below 0.5 $mW/(m^2 \cdot sr \cdot cm^{-1})$ in the long-wave band **(Li et al., 2022b)**.Additionally, Fig. 2(b) compares the absorption features of SO_2 (with an assumed altitude of 15 km) against those of major interfering gases (O_3, CO_2, and H_2O) within the selected spectral window. This radiative transfer simulation is based on an ERA5 atmospheric profile from a representative point during the GIIRS observation. The results show that SO_2 exhibits distinct absorption characteristics compared to these interfering species, providing a physical basis for retrievals by using the available weak absorption features. The radiative transfer model is described in Section 3.

2.2.2 GEMS

The Geostationary Environment Monitoring Spectrometer (GEMS), launched in February 2020 aboard the South Korean GK-2B satellite, is the world's first geostationary ultraviolet-visible spectrometer **(Kim et al., 2020)**. It provides hourly SO_2 column observations with a high spatial resolution of 3.5 km × 7.7 km at Seoul, Korea, covering the East Asian region (5°S–45°N,

https://doi.org/10.5194/egusphere-2026-1745
Preprint. Discussion started: 16 April 2026

75°E–145°E). This study utilizes the GEMS v2.1 SO_2 vertical column density product, which is retrieved using a hybrid algorithm of Differential Optical Absorption Spectroscopy (DOAS) and Principal Component Analysis (PCA). To maintain spatial continuity for SO_2 mass loading calculations, a relaxed filtering criterion is applied, specifically limiting both the solar zenith angle and viewing zenith angle to less than 70°. Further details regarding data screening, such as the impact of cloud fraction thresholds (< 0.7) based on Algorithm Theoretical Basis Document (ATBD) **(Lee et al., 2024)** recommendations, are provided in Section 5.2.2.

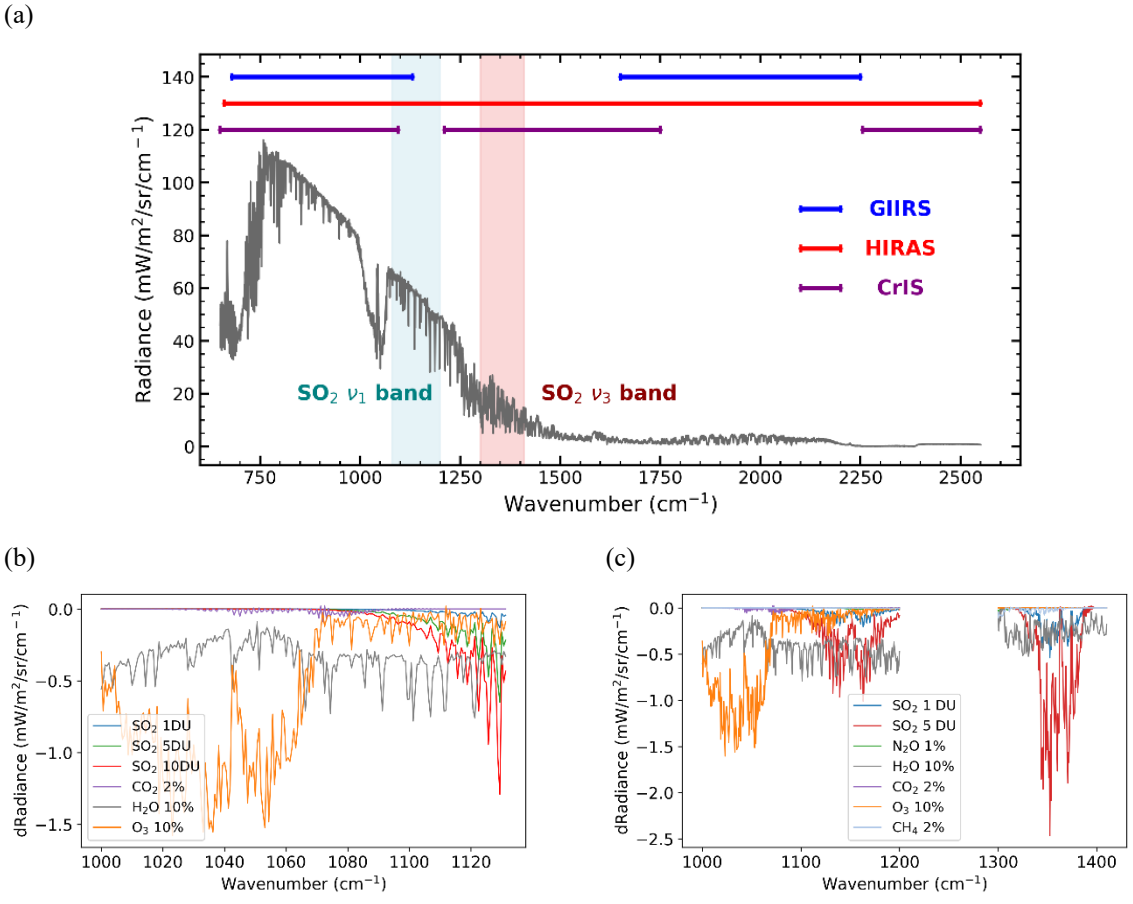

Figure 2: (a) A full-band long-wave infrared spectrum (HIRAS). The top horizontal bars indicate the full spectral coverage of the three sensors, while the shaded regions highlight the fundamental SO_2 *ν*1 and *ν*3 absorption features. (b, c) Radiative transfer simulations comparing the absorption features of SO_2 (assumed at 15 km altitude) with major interfering gases. Panel (b) corresponds to the GIIRS retrieval window (1000–1131.25 cm^{-1}), while panel (c) corresponds to the HIRAS retrieval windows (1000–1200 cm^{-1} and 1300–1410 cm^{-1}). Both simulations are based on an ERA5 atmospheric profile from a representative point during their respective overpasses.

https://doi.org/10.5194/egusphere-2026-1745
Preprint. Discussion started: 16 April 2026

2.3 Polar-Orbiting Satellite Observations

2.3.1 HIRAS

The second-generation Hyperspectral Infrared Atmospheric Sounder (HIRAS-II) is deployed on the FY-3E and FY-3F platforms, featuring a nadir spatial resolution of 14 km and a spectral resolution of 0.625 cm^{-1}. FY-3E operates in a dawn/dusk orbit with a local equatorial overpass time of approximately 05:30 AM/PM, while FY-3F follows a morning orbit with an overpass time of around 10:00 AM/PM **(Zhang et al., 2022)**. The SO_2 retrieval algorithm for HIRAS generally follows the method described by **Zeng et al. (2025)**. For the spectral window selection, we adopted the strategy of **Carboni et al. (2012)**, utilizing both the strong $\nu 3$ band (1300–1410 cm^{-1}) and the weak $\nu 1$ band (1000–1200 cm^{-1}), as explicitly denoted in Fig. 2(a). Figs. S1(c) and (d) present the mean spectra and corresponding NEdR for HIRAS observations over the potential plume area (20°W–140°E，5°S–25°N) on June 2, 2024. The mean NEdR is below 0.3 mW/(m^2·sr·cm^{-1}) in the $\nu 1$ band and further decreases to less than 0.1 mW/(m^2·sr·cm^{-1}) in the $\nu 3$ band, demonstrating excellent signal-to-noise performance. The radiative transfer simulations (Fig. 2c), driven by a local ERA5 profile during the HIRAS overpass, highlight the unique spectral signatures of SO_2 in these bands, providing a foundation for the physical retrieval process.

2.3.2 CrIS

The Cross-track Infrared Sounder (CrIS), also a Fourier transform Michelson interferometer, provides hyperspectral infrared measurements with a spectral resolution of 0.625 cm^{-1} and a nadir spatial resolution of approximately 14 km. CrIS was initially launched aboard S-NPP in 2011, subsequently deployed on JPSS-1 (2017) and JPSS-2 (2022). The local equatorial overpass time of approximately 01:30 AM/PM, with a difference of tens of minutes between different satellites **(Han et al., 2013)**. As shown in Fig. 2(a), the CrIS long-wave band truncates at about 1095 cm^{-1}. Consequently, the physical retrieval algorithm employed for CrIS Level-1 spectra follows the same framework as that for HIRAS; but only constrained to the $\nu 3$ band (1300–1410 cm^{-1}). Figs. S1(e) and (f) show the mean observed spectra and corresponding NEdR for the study area. The NEdR remains below 0.05 mW/(m^2·sr·cm^{-1}), indicating an exceptional signal-to-noise ratio.

2.3.3 IASI

The Infrared Atmospheric Sounding Interferometer (IASI) is an hyperspectral infrared instrument deployed on the Metop-A (2006), Metop-B (2012), and Metop-C (2018) platforms **(Clerbaux et al., 2009)**. IASI provides continuous spectral coverage from 645 to 2760 $cm^{-1}$with a spectral resolution of 0.25 cm^{-1} (0.5 cm^{-1} after apodization). At a reference temperature of 280 K, the Noise Equivalent differential Temperature (NEdT) in the $\nu 3$ and $\nu 1$ bands is 0.05 K and 0.12 K, respectively. The instrument has a circular nadir footprint of 12 km in diameter and a local equatorial overpass time of 09:30 AM/PM. The retrieval of SO_2 columns and plume heights from IASI is documented in **Clarisse et al. (2026)**. This study utilizes the IASI SO_2 v4.5 products from Metop-B and Metop-C.

https://doi.org/10.5194/egusphere-2026-1745
Preprint. Discussion started: 16 April 2026

2.3.4 TROPOMI

The TROPOspheric Monitoring Instrument (TROPOMI), aboard the Sentinel-5P satellite launched in October 2017, is a hyperspectral nadir-viewing spectrometer with a local equatorial overpass time of 01:30 PM. It measures radiation across ultraviolet, visible, near-infrared, and short-wave infrared bands, featuring a current spatial resolution of 3.5 km × 5.5 km **(Veefkind et al., 2012)**. We employ the SO_2 v02 product generated by the Covariance-Based Retrieval Algorithm (COBRA, **Theys et al., 2021**). Compared to conventional DOAS techniques, COBRA significantly reduces noise and bias while enhancing sensitivity to low SO_2 concentrations. Data based on a 15 km plume height a priori assumption with both the solar zenith angle and viewing zenith angle less than 70° are selected for analysis.

2.3.5 MLS

The Microwave Limb Sounder (MLS) aboard the Aura satellite was launched in July 2004, with a local equatorial overpass time of approximately 01:30 AM/PM **(Waters et al., 2006).** The standard SO_2 product is retrieved from the 240 GHz band, specifically targeting enhanced SO_2 signals such as volcanic plumes. The verification of SO_2 products can be found in **Pumphrey et al. (2015)**. This study incorporates the Version 5 SO_2 dataset. Following the MLS Version 5 data quality documentation **(Livesey et al., 2022)**, only profile data within the pressure range of 215 hPa to 10 hPa (~14–32 km) with quality factors greater than 0.95 are used. In this effective range, the estimated precision is approximately 4 ppbv, with an accuracy between 10 and 20 ppbv.

3 Methodology

This section details the physical retrieval algorithm developed for volcanic SO_2 monitoring. The algorithm is applied to the Level-1 spectral data from FY-4B/GIIRS, FY-3E/F HIRAS, and JPSS-1/2 CrIS to generate SO_2 total column and plume heights. The Fengyun Geostationary and Low-earth-orbit Atmospheric Infrared Retrieval (FY-GeoAIR/FY-LeoAIR) algorithms serve as the fundamental radiative transfer framework for this study **(Zeng et al., 2023a)**. Detailed configurations of the forward model are provided in the Supplementary Materials.

3.1 SO_2 plume detection and layer height estimation

The detection of volcanic SO_2 plumes and the estimation of layer height in this study are based on the Hyperspectral Range Index (HRI) method. This method features high sensitivity and computational efficiency and has been applied to the detection of SO_2 and other weakly absorbing atmospheric substances **(e.g., Walker et al., 2011; Carboni et al., 2012; Clarisse et al., 2014; Zeng et al., 2025)**. The core principle involves quantifying target gas absorption intensity by projecting the observed spectra onto pre-calculated SO_2 spectral features (Jacobians) within a covariance-weighted space. The HRI is defined as:

$$\mathbf{HRI} = \frac{\mathbf{K^T S^{-1}}(\boldsymbol{y}-\bar{\boldsymbol{y}})}{\sqrt{\mathbf{K^T S^{-1} K}}} \quad (1)$$

https://doi.org/10.5194/egusphere-2026-1745
Preprint. Discussion started: 16 April 2026

where **K** represents the SO_2 Jacobian vector (the partial derivative of radiance with respect to the SO_2 total column), $\boldsymbol{y}$ is the observed spectrum, and $\bar{\boldsymbol{y}}$ is the mean background spectrum. The background covariance matrix **S** is constructed from random spectra samples unaffected by SO_2 to account for interference from poorly constrained or unknown atmospheric parameters. For a population of spectra without observable enhancement of SO_2, the HRI distribution exhibits a mean of zero and a standard deviation of one. Higher HRI values indicate a greater likelihood of SO_2 enhancement.

In this work, the HRI method is implemented across three different hyperspectral infrared sounders. The specific spectral bands employed for each instrument have been detailed in Section 2. The background fields ($\bar{\boldsymbol{y}}$ and **S**) are derived from respective observations on June 2, 2024 (the day prior to the eruption), within the potential unpolluted volcanic plume regions (20°W to 140°E, 5°S to 25°N for HIRAS and CrIS; 70°W to 140°E, 0°N to 20°N for GIIRS). The Jacobian **K** is generated using the FY-LeoAIR and FY-GeoAIR algorithm via finite difference calculations based on a SO_2 column of approximately 1 DU (10 times the a priori). It is noted that the effectiveness of this HRI-based method relies heavily on the accurate construction of covariance matrix **S**, which is required to accurately represent the unpolluted atmospheric background and instrumental noise characteristics. Furthermore, intense water vapor absorption in the $\nu 3$ band limits infrared sensitivity to SO_2 within the lower troposphere, thus the observed signals primarily originate from the upper troposphere and even the stratosphere. However, explosive volcanic eruptions typically inject massive amounts of SO_2 into higher altitudes (often exceeding 10 km). At these levels, hyperspectral infrared observations maintain high sensitivity to the SO_2 plume.

Building upon the initial detection, the SO_2 layer height is determined by quantifying the matching degree between the observed spectra and theoretical SO_2 spectral features at various altitudes. This is achieved by extending Equation (1) to a height-dependent index, $\mathbf{HRI}(\boldsymbol{h})$, in which the Jacobian **K** is substituted with an altitude-dependent Jacobian matrix $\mathbf{K}_{\boldsymbol{h}}$. The implementation involves using the FY-LeoAIR radiative transfer model to pre-calculate $\mathbf{K}_{\boldsymbol{h}}$ for different altitude layers ranging from 2 to 25 km at 1 km intervals, using a constant SO_2 column density of 10 DU for each layer. The estimated plume height $\boldsymbol{h}$ is identified at the point where $\mathbf{HRI}(\boldsymbol{h})$ reaches its maximum value, signifying the optimal match between the observations and the theoretical forward model **(Clarisse et al., 2014)**.

For this height estimation step, the spectral window is restricted exclusively to the strong $\nu 3$ band (1300–1410 cm^{-1}). This band overlaps with strong water vapor absorption, which provides the necessary altitude-dependent interference to effectively resolve the SO_2 layer height. Consequently, the $\mathbf{HRI}(\boldsymbol{h})$ utilizes a new covariance matrix and mean spectrum constructed solely over this restricted $\nu 3$ range. Notably, the SO_2 layer height for the FY-4B/GIIRS observations is constrained using the retrieval results from the synergistic HIRAS and CrIS. Direct height retrieval from GIIRS spectra proved challenging due to its restricted spectral coverage, which only encompasses the weaker SO_2 $\nu 1$ band. Regarding the performance, the height retrieval method demonstrates robust performance under cloudy conditions. According to **Clarisse et al. (2014)**, retrieval errors generally remain below 2 km, provided that clouds do not completely obscure the underlying SO_2 layer. However, its sensitivity decreases for saturated plumes with exceptionally high SO_2 concentrations, while recent developments have improved this specific issue **(Clarisse et al., 2026)**.

https://doi.org/10.5194/egusphere-2026-1745
Preprint. Discussion started: 16 April 2026

3.2 Retrieval of SO_2 total column

This study presents a full physical retrieval algorithm for volcanic SO_2 column densities grounded in optimal estimation method **(Rodgers, 2000)**, following the frameworks established by **Carboni et al. (2012)** and **Zeng et al. (2025)**. Instead of explicitly solving for every atmospheric parameter influencing the spectra, the algorithm treats unknown atmospheric interferences (e.g., water vapor variability and cloud effects) as generalized uncertainty sources. Their spectral effects are encapsulated within a comprehensive error covariance matrix ($\mathbf{S}_{\boldsymbol{\varepsilon}}$). This strategy significantly simplifies the retrieval system. Under a quasi-linear assumption, this formulation is mathematically equivalent to the simultaneous retrieval of all interfering parameters **(Von Clarmann et al., 2001)**. The solution is achieved by minimizing the following cost function:

$$\boldsymbol{J}(\boldsymbol{x}) = [\boldsymbol{y} - \mathbf{F}(\boldsymbol{x}, \boldsymbol{b})]^T \mathbf{S}_{\boldsymbol{\varepsilon}}^{-1} [\boldsymbol{y} - \mathbf{F}(\boldsymbol{x}, \boldsymbol{b})] + (\boldsymbol{x} - \boldsymbol{x}_a)^T \mathbf{S}_{\boldsymbol{a}}^{-1} (\boldsymbol{x} - \boldsymbol{x}_a), \quad (2)$$

where $\boldsymbol{y}$ is the observation vector, $\mathbf{F}(\boldsymbol{x}, \boldsymbol{b})$ denotes the forward radiative transfer model used to simulate theoretical spectra based on the state vector $\boldsymbol{x}$ (comprising SO_2 column density and surface temperature) and a set of fixed parameters $\boldsymbol{b}$ (e.g., viewing geometry, surface emissivity, and pre-defined trace gas profiles). Specifically, the interfering gases accounted for include H_2O, O_3, CH_4, N_2O and HNO_3. $\boldsymbol{x}_a$ represents the a priori state vector, and $\mathbf{S}_{\boldsymbol{a}}$ is the a priori covariance matrix which quantifies the constraint strength applied to the initial guess, assumed here to be diagonal. To ensure the retrieval is primarily observation-driven and to minimize the influence of potentially inaccurate a priori information, we employ weak constraints: the a priori uncertainties are set to 500% for the SO_2 column density and 20 K for the surface temperature.

The performance of the algorithm depends on the construction of $\mathbf{S}_{\boldsymbol{\varepsilon}}$, which is derived by statistically characterizing the residuals between observed and simulated spectra in SO_2-free scenarios. Simulated spectra are generated by using multi-instrument observations from June 2, 2024 and ERA5 reanalysis data as model inputs while fixing the SO_2 concentration at zero. The resulting residual covariance matrix effectively encapsulates the combined influence of instrumental noise, forward model errors, and the variability of unresolved atmospheric parameters (e.g., interfering gases and thin clouds), while ensuring that SO_2 spectral features are excluded. The selection of background regions for $\mathbf{S}_{\boldsymbol{\varepsilon}}$ follows the strategy detailed in Section 3.2. The minimization of the cost function $\boldsymbol{J}(\boldsymbol{x})$ is performed using the Levenberg-Marquardt iterative solver. The posterior error covariance matrix of the retrieved state estimate is expressed as:

$$\hat{\mathbf{S}} = (\mathbf{K}^{\mathbf{T}} \mathbf{S}_{\boldsymbol{\varepsilon}}^{-1} \mathbf{K} + \mathbf{S}_{\boldsymbol{a}}^{-1})^{-1}. \quad (3)$$

4 Observation simulated experiments

Before applying the physical retrieval algorithm to actual satellite data, simulation experiments using synthetic spectra are conducted to evaluate the efficacy and sensitivity of the SO_2 retrieval algorithm. The atmospheric scenarios are constructed using ERA5 reanalysis data, and synthetic observations are generated using the forward model described in Section 3. Synthetic spectra are simulated by adding Gaussian noise based on the NEdR of each respective instrument to the simulated radiances. The retrieval is then performed using the algorithm described in Section 3.2. In the experiments, the "true" SO_2 total column ranges from 0.5 to 50 DU, with plume altitude sets between 7 and 15 km. To ensure statistical representativeness,

https://doi.org/10.5194/egusphere-2026-1745
Preprint. Discussion started: 16 April 2026

approximately 1000 sample points are extracted at equal intervals from the potential plume regions observed by GIIRS and HIRAS on June 2, 2024, respectively, to build the simulation datasets.

Figs. 3a and 3b compare retrieved values with true values for GIIRS and HIRAS, respectively, with gray points representing the initial guess (fixed at ~1 DU). The results show a high overall consistency, particularly with a correlation coefficient (r) approaching 1.00. It is important to clarify that this near-perfect correlation represents a theoretical upper limit. Because this simulation aims only to verify the mathematical soundness and robust convergence of the retrieval algorithm under noise-only scenarios, uncertainties related to aerosol scattering, sub-pixel cloud contamination, and spectroscopic uncertainties are not considered.

Despite this idealized setup, distinct performance differences emerge between the sensors due to their spectral coverage. For HIRAS, retrieval errors remained below 1 DU in most cases. For GIIRS, due to limited spectral coverage, SO_2 columns are generally underestimated by more than 20%. However, it demonstrates effective sensitivity to high concentrations, e.g., retrieving ~37 DU for a 50 DU true value, significantly higher than the initial guess (1 DU). Error analysis (Figs. 3c, d) indicates that both percentage errors and posterior uncertainties decrease as plume altitude and SO_2 loading increase. The smallest errors occur under high-altitude and high-concentration conditions, consistent with the findings of **Carboni et al. (2012)**. The experiments also identified the GIIRS theoretical detection limit: at a concentration of 3 DU and 10 km altitude, retrieval errors exceed 100%, which represents a lower bound for the real-world detection threshold.

While this study does not explicitly treat interference from clouds or volcanic ash, their impacts are characterized in the simulation experiments of **Carboni et al. (2012)**. The presence of clouds or volcanic ash within or above the SO_2 plume attenuates the spectral signal, leading to underestimation, whereas their presence below the plume has a negligible effect. Developing simultaneous retrieval algorithms for SO_2, ash, and clouds remains a key future direction.

https://doi.org/10.5194/egusphere-2026-1745
Preprint. Discussion started: 16 April 2026

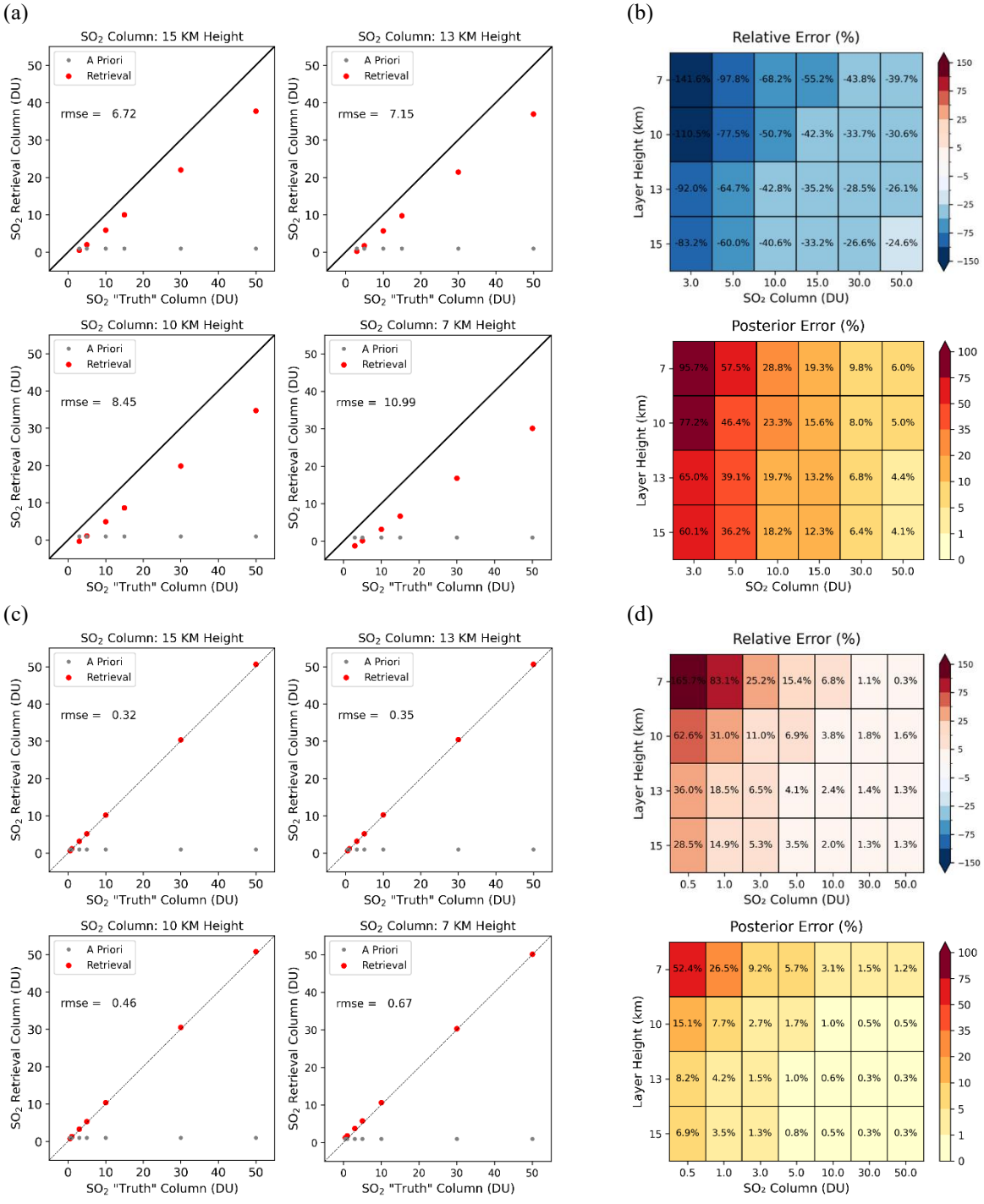

Figure 3: Performance evaluation of the physical retrieval algorithm based on synthetic spectral experiments. (a, c) Comparison between retrieved and true SO_2 total column for (a) FY-4B/GIIRS and (c) FY-3E/F HIRAS, where gray dots represent the a priori initial guesses. (b, d) Retrieval errors and posterior uncertainties as a function of plume altitude and for SO_2 column for (b) FY-4B/GIIRS and (d) FY-3E/F HIRAS.

https://doi.org/10.5194/egusphere-2026-1745
Preprint. Discussion started: 16 April 2026

5 Results and discussion

5.1 Case study: Kanlaon volcano eruption in June 2024

Mt. Kanlaon (10.4°N, 123.1°E; 2,422 m), a stratovolcano on Negros Island, Philippines, experienced a six-minute explosive eruption (VEI 2) at 18:51 local time on June 3, 2024, according to the **Global Volcanism Program (2025)**. The event caused widespread ashfall and necessitated the evacuation of over 1,800 residents. While its total SO_2 loading was less than 1% of the 1991 Mt. Pinatubo eruption (~20 Tg), such moderate-scale events are highly representative of the frequent volcanic activity in Southeast Asia. This eruption serves as an ideal testbed for geostationary hyperspectral infrared sensing and GEO-LEO synergistic observations.

5.2 SO_2 retrievals from the GEO satellite constellation

5.2.1 GIIRS

Fig. S2 illustrates the LWIR brightness temperature (BT) spectra acquired by FY-4B/GIIRS at 16.3 UTC on June 3, 2024 (~5.5 hours post-eruption). A comparison between a pixel inside the volcanic plume (black) and an adjacent clean-air pixel (red) reveals two primary spectral fingerprints. First, a significant enhancement in absorption is observed within the 700–1000 cm^{-1} range, particularly the strong absorption valley near 800 cm^{-1}, which is attributed to the combined radiative effects of ice crystals and volcanic ash **(Clarisse & Prata, 2016)**. Second, within the SO_2 ν1 weak absorption band (1070–1130 cm^{-1}), the in-plume spectra exhibit a clear absorption trough, with the differential BT (ΔBT = BT_in − BT_out, in Fig. S2b) showing negative values, confirming the presence of SO_2.

To track the spatio-temporal evolution of the SO_2 plume, we calculate HRI for GIIRS observations. Fig. 4 shows the HRI distribution for 8 overpasses within the first 15 hours post-eruption (22 h LT data missing). The first overpass (20 h LT, ~1 hour post-eruption) shows the plume concentrated near the volcano with a small spatial range and high HRI. By 0 h LT on June 4, the plume morphology changes with two separated high-value areas: one rapidly transports southwestward, while the other remains stagnant near the volcano before gradually dispersing. Subsequent GIIRS overpasses (see Fig. S3) show the main plume body continuing to migrate southwest and diluting, consistent with other satellite results. However, these observations are excluded from quantitative retrieval due to degraded signal-to-noise ratios and low HRI values.

A differentiated pixel screening scheme is implemented prior to retrieval to remove false positives and improve computational efficiency. For polar-orbiting sensors (HIRAS and CrIS), a strict threshold (HRI > 5) is applied. For GIIRS, which possesses lower detection sensitivity, a three-step strategy is developed: (1) an initial pre-screening with a relaxed threshold (HRI > 1); (2) spatial masking using synergistic multi-source observations, e.g., HIRAS, (time lag < 1 h); and (3) temporal interpolation of plume boundaries for periods lacking synergistic data. Specifically, in step (3), we extract the plume boundary polygons from adjacent time steps with available synergistic data. The Hungarian algorithm **(Kuhn, 1955)** is then applied to optimally match the boundary points between these sequential polygons. Finally, time-weighted linear interpolation is performed on the matched points to reconstruct the plume's spatial mask for the target intermediate time.

https://doi.org/10.5194/egusphere-2026-1745
Preprint. Discussion started: 16 April 2026

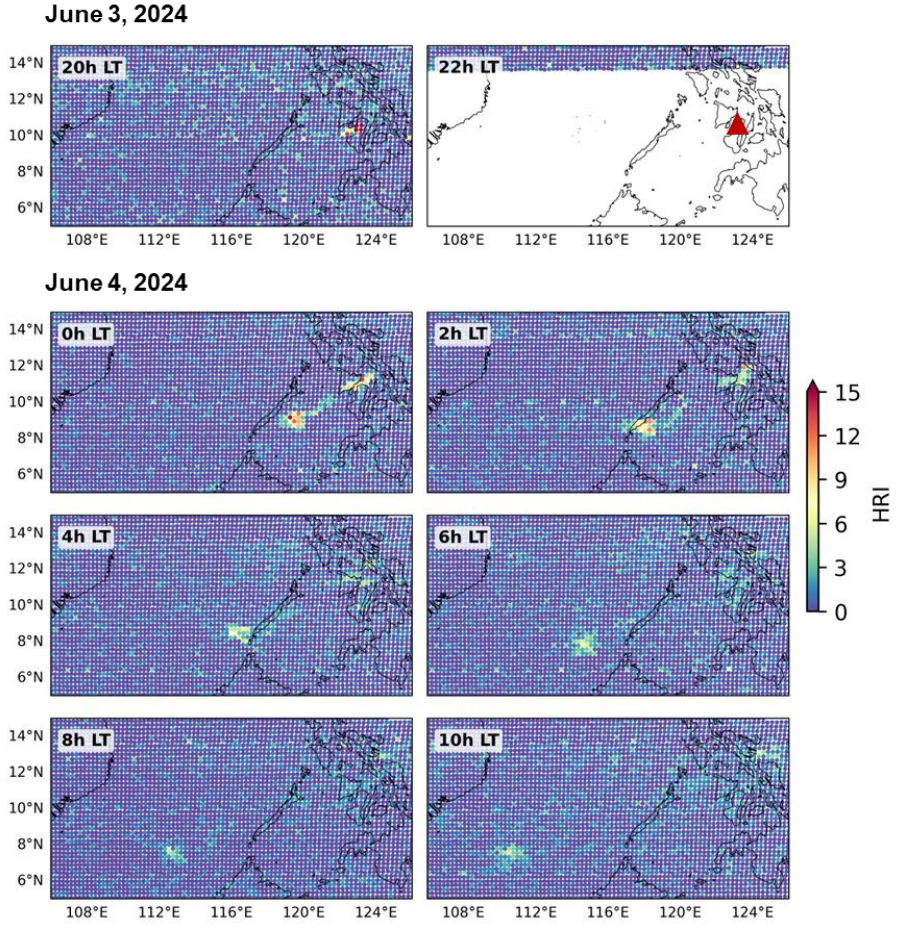

Figure 4: Spatial distribution of the SO_2 HRI calculated from FY-4B/GIIRS spectra during the first 15 hours after the eruption. The red triangle in the overpass at 22h LT marks the location of the Kanlaon volcano (10.4°N, 123.1°E).

SO_2 total columns (Figs. 5 and S5) are then retrieved from GIIRS spectra using plume height constraints derived from HIRAS and CrIS, with the corresponding layer height distributions of GIIRS shown in Fig. S4. To highlight concentration trends, Fig. 5 employs a uniform 0–20 DU color scale, whereas Fig. S5 provides independent scales to display the absolute concentrations for each observation. The estimated posterior error for the SO_2 column is 53.7 $\pm$ 24.1%, shown in Fig. S6.

GIIRS captures the earliest SO_2 signal among all platforms (~1 h post-eruption, 20h LT), peaking at 118 DU near the crater (Fig. S5). The subsequent sequence reveals a divergence in plume evolution. By 0 h LT on June 4, the plume split into two distinct centers (~42 DU). The western plume (14–16 km) shows rapid southwestward transport with a clear monotonic decrease in peak concentration from 0h to 10h LT (30 → 21 → 17 → 15 → 14 DU). Reaching near the local tropopause, this plume likely corresponds to the upper portion of the initial explosive column, carried by strong upper-level winds. Conversely, the eastern plume (9–12 km) exhibits slower, irregular dispersion with non-monotonic fluctuations (42→ 35→ 32→ 20→ 13→ 18 DU), likely representing the middle portion of the initial eruption column. The concentration fluctuations observed

https://doi.org/10.5194/egusphere-2026-1745
Preprint. Discussion started: 16 April 2026

here could be attributed to the spatial undersampling of GIIRS (~12 km inter-pixel gaps) occasionally missing the concentrated core, as well as variable wind fields at these altitudes causing unstable transport. In summary, GIIRS provides the earliest quantitative record and, through continuous monitoring, reveals the 3D differentiation of the plume, offering a unique perspective on the initial transport and evolution of volcanic materials.

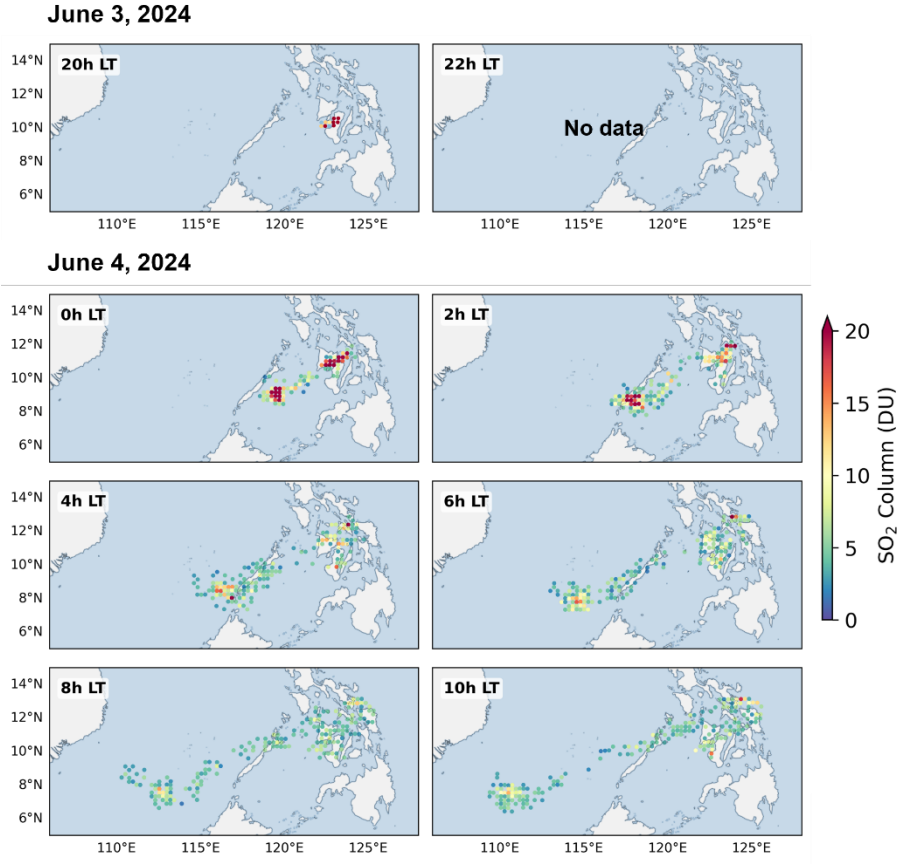

Figure 5: Spatiotemporal evolution of volcanic SO2 total column retrieved from FY-4B/GIIRS, corresponding to HRI maps shown in Fig. 4.

5.2.2 GEMS

GEMS provides continuous SO_2 plume observations on June 4 (about 1–8 h UTC) and June 5 (5–8 h UTC), which complements the FY-4B/GIIRS monitoring, forming a high-temporal-resolution geostationary sequence covering ~20 hours of the early post-eruption phase. Notably, official GEMS SO_2 products utilize an a priori profile derived from a chemical transport model, which differs significantly from actual volcanic plume conditions and the 15 km fixed-height assumption used by TROPOMI. This discrepancy directly introduces a systematic overestimation. To address this, TROPOMI SO_2 products are used as a benchmark for bias correction. Both datasets are first regridded to a 0.5° spatial resolution and subjected to low-value filtering. By analyzing the spatiotemporally matched grid points within a 30-minute observation window (Figs.

https://doi.org/10.5194/egusphere-2026-1745
Preprint. Discussion started: 16 April 2026

S7a, S7c), we derived an empirical scaling factor of 0.5 that effectively eliminates systematic overestimation (Figs. S7b, S7d). For instance, at 5 h UTC on June 4, the RMSE decreases from 1.66 to 0.43 DU and the regression slope improves from 1.90 to 0.95 after correction, confirming high data reliability.

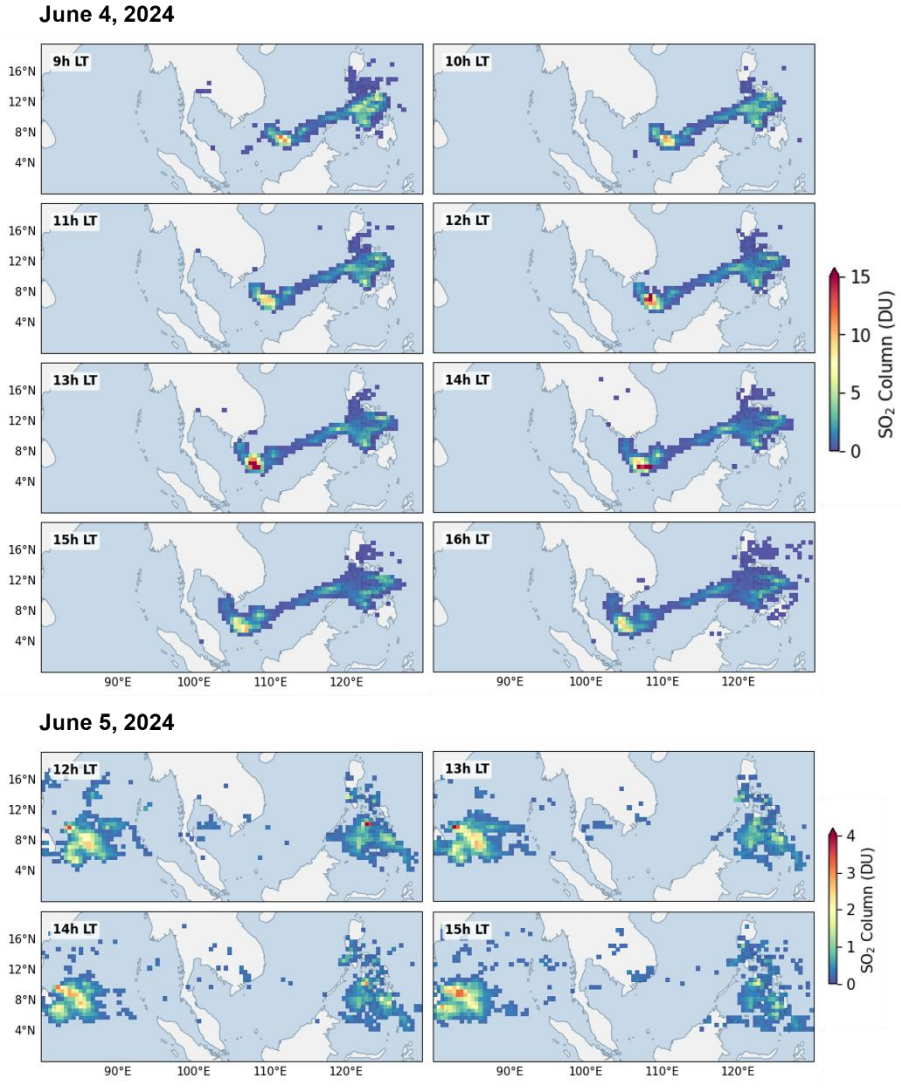

Figure 6: Daytime spatiotemporal evolution of bias-corrected SO_2 total column from GEMS during June 4–5, 2024.

Corrected GEMS data reveal the daytime evolution of the plume (Fig. 6): the western component adverts rapidly southwestward, while the eastern component diffuses slowly near the crater. Notably, the SO_2 columns in the eastern plume are lower than those from infrared observations, and anomalously high values appear in the western plume during 4–6 h UTC. These discrepancies are likely attributed to the inaccurate plume height assumptions and observational interference by cloud cover. To address the cloud effects, sensitivity tests are conducted using a cloud fraction threshold (< 0.7) as recommended by algorithm documentation. However, this cloud screening removes many SO_2 pixels, compromising the spatial integrity of the

https://doi.org/10.5194/egusphere-2026-1745
Preprint. Discussion started: 16 April 2026

plume and leading to a systematic underestimation of the total mass. Therefore, the primary results in this study are based on pixels without cloud filtering, with cloud-screened results provided in the supplementary information (see Fig. S26).

Excluding isolated anomalies, the western plume concentration steadily declines from ~12 DU (1 h UTC) to 9.5 DU (8 h UTC), indicating continuous dilution. GEMS observations on June 4 capture the critical window when the total SO_2 mass likely reaches its peak (see Section 5.4). By June 5, the western plume travels over 20 degrees of longitude and disperses, while the eastern component dissipates completely—a divergence likely driven by wind fields at different injection altitudes. Overall, the GEMS sequence provides a continuous daytime record that effectively captures the rapid dispersion and progressive dilution of the volcanic plume.

5.3 SO_2 retrievals from the LEO satellite constellation and cross-comparisons

5.3.1 HIRAS and CrIS

This section utilizes a polar-orbiting infrared constellation comprising FY-3E/F HIRAS and JPSS-1/2 CrIS, achieving 6 daily overpasses through varied equatorial crossing times. HRI results from June 3 to 8, 2024 confirm the effective identification of the SO_2 plume (Figs. S8 and S9). Based on a screening threshold of HRI > 5, the plume heights are retrieved (Figs. S10–S14). The retrieved heights show high consistency across sensors and reveal significant differences in the vertical structure and lifetime between the eastern and western plumes. The western plume rapidly ascends to 14–16 km on June 4 and remains stable during its multi-day transoceanic transport. In contrast, the eastern plume is confined to lower altitudes (5–12 km) and dissipates by around June 5. This shorter lifetime likely results from rapid meteorological dispersion or the plume sinking below the infrared detection threshold (~5 km). The western component stabilizes beneath the tropical tropopause (~17 km), indicating that the injected SO_2 did not penetrate the stable stratification into the stratosphere.

SO_2 total column results are presented in Figs. 7 and S15 (uniform 0–5 DU scale), while early eruption high-concentration observations from FY-3F/HIRAS and CrIS are displayed with independent scales in Figs. S18 and S16. Additionally, complete retrieval total columns for JPSS-1/2 CrIS are provided in Fig. S16. Quantitative analysis shows that the first LEO overpass (FY-3F/HIRAS, 1.5 h after GIIRS's first detection) captures a peak concentration of 78 DU (only converged pixels). Subsequent observations by CrIS and FY-3E/HIRAS document the rapid decay of the western plume core from ~44 DU to 20 DU, eventually falling below 0.5 DU as the plume dispersed over Africa by June 8. This comprehensive decay record highlights the global coverage of LEO satellites, which effectively supplements the spatial limitation of GEO sensors for fixed field of view. Nevertheless, LEO observations are constrained by inherent drawbacks, including swath gaps and low revisit frequencies (1 or 2 per day for single platform, significantly lower than 12 per day for GIIRS).

Cross-validation of GIIRS retrievals using LEO observations is presented in Figs. 8 and S17. Fig. 9 compares GIIRS with the temporally closest FY-3E/F HIRAS overpasses. Since GIIRS's spectral coverage is limited to the weak SO_2 absorption band, it is insensitive to low SO_2 concentrations and possesses effective detection capability only for high-loading areas. Consequently, the remaining retrieving points are discrete and scarce; however, they show good agreement with HIRAS in

https://doi.org/10.5194/egusphere-2026-1745
Preprint. Discussion started: 16 April 2026

high-value regions (red circles, Fig. 8). For fair comparison, pixels with SO_2 concentration below 2.5 DU are excluded for all sensors, and data are averaged onto 0.5° by 0.5° grids. The resulting scatter plots yield correlation coefficients of 0.74 and 0.84, indicating good consistency. Furthermore, while significant observation time lags and resultant plume displacements make it unfair to perform point-to-point grid comparisons with IASI and CrIS (Fig. S17), the consistent spatial distribution features across different sensors visually validate the reliability of the retrievals.

https://doi.org/10.5194/egusphere-2026-1745
Preprint. Discussion started: 16 April 2026

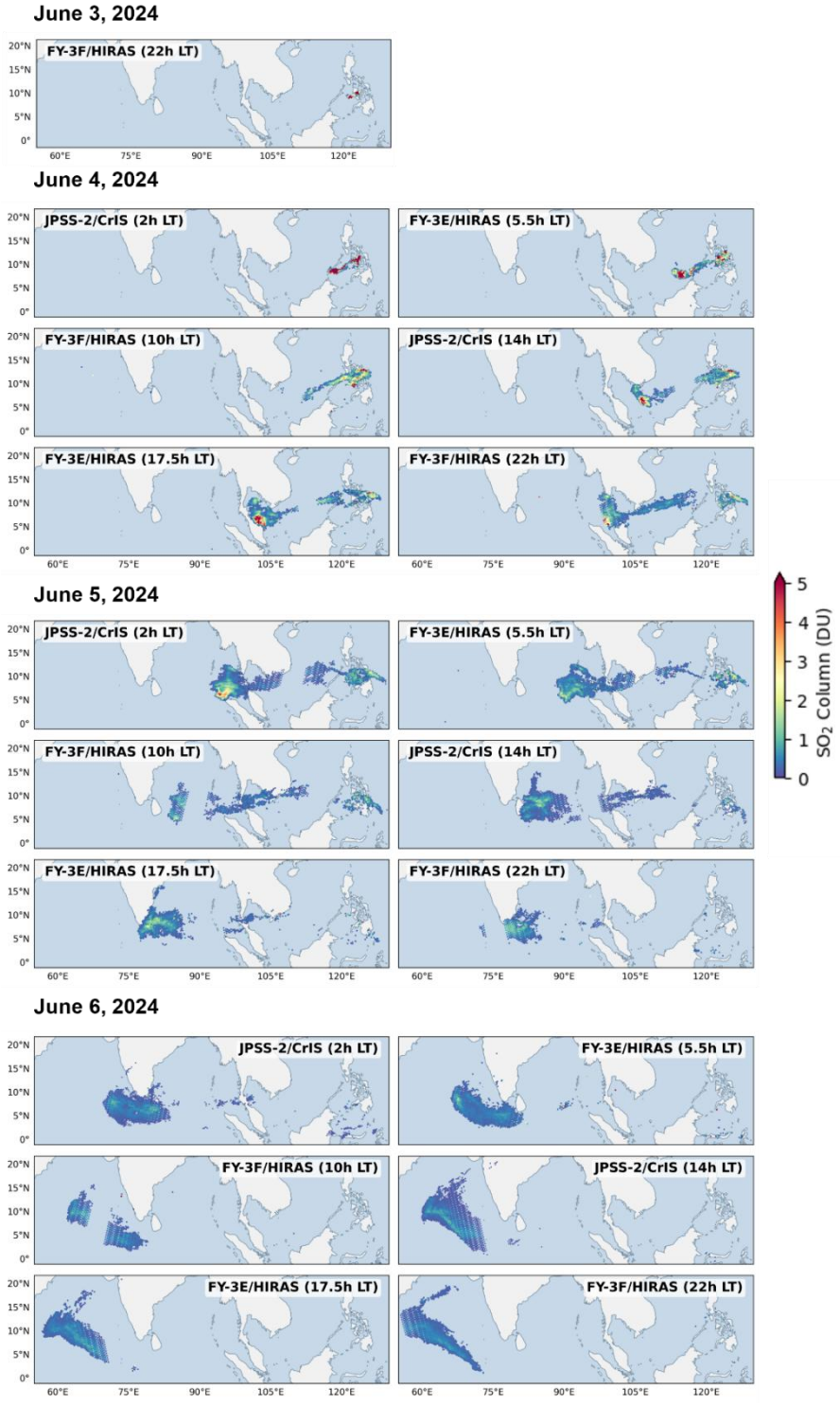

Figure 7: Spatiotemporal evolution of volcanic SO_2 total columns retrieved from FY-3E/F HIRAS and JPSS-2 CrIS during June 3–6, 2024.

https://doi.org/10.5194/egusphere-2026-1745
Preprint. Discussion started: 16 April 2026

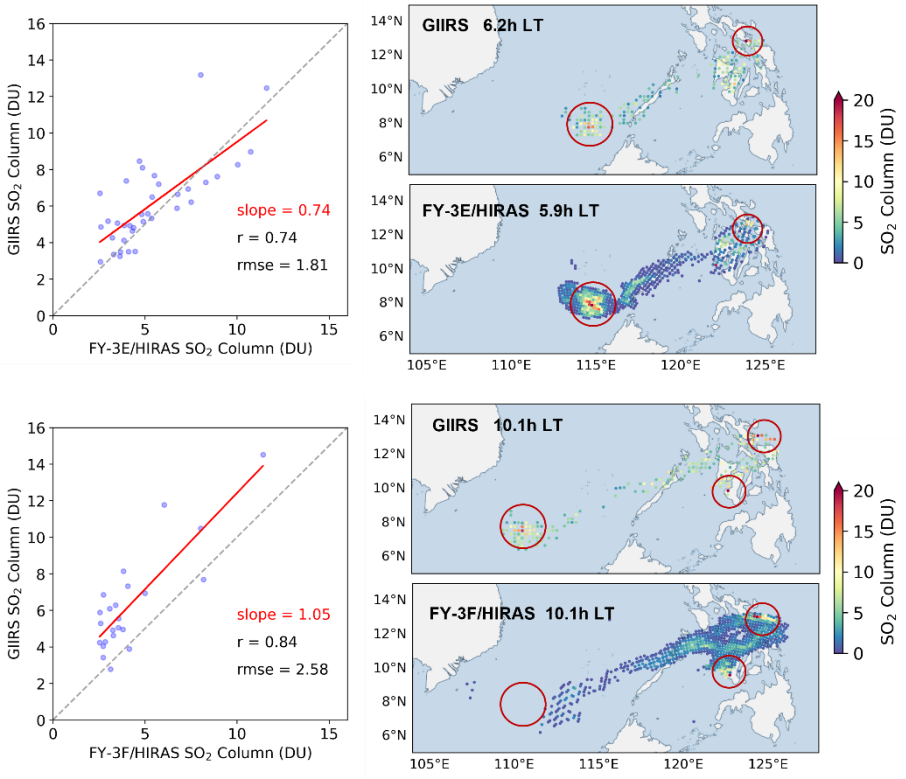

Figure 8: Cross-validation of FY-4B/GIIRS SO_2 total columns against the temporally closest FY-3E/F HIRAS observations. Red circles indicate high-loading regions. The scatter plots display the point-to-point comparisons based on gridded data (0.5° by 0.5° grids).

5.3.2 IASI, TROPOMI and MLS

To further complete the synergistic observation framework and provide independent validation for our retrieval algorithm, this study incorporates L2 products from Metop-B/C IASI (IR) and Sentinel-5P TROPOMI (UV).

All comparison datasets are resampled to 0.5° by 0.5° grids for point-to-point analysis. Fig. 9a illustrates a comparison instance between IASI and FY-3F/HIRAS at approximately 22h LT on June 4, 2024, with additional matched observation pairs provided in Figs. S18 and S19. To further evaluate the algorithm's performance, a statistical analysis was conducted by aggregating all matched data points throughout the study period (Fig. 9b). The results show a high correlation of 0.78 and an RMSE of 0.27 DU, demonstrating good consistency between HIRAS and the IASI products. The discrepancies observed at certain timestamps likely stem from non-synchronous overpasses (with time lags of several tens of minutes), which exert a more pronounced impact on such small-scale and rapidly evolving volcanic plumes. In addition, the spatial distributions of IASI SO_2 plume heights are provided in Figs. S20 and S21. Statistical assessment across the respective overpasses reveals that IASI heights are systematically higher than those from FY-3F/HIRAS, with mean values being 0.2–1.6 km higher and medians exhibiting a positive offset of 1–2 km. Such height discrepancies have been reported by Zeng et al. (2025). They are likely due

https://doi.org/10.5194/egusphere-2026-1745
Preprint. Discussion started: 16 April 2026

to the effects of inherent instrumental differences and distinct retrieval algorithms. The temporal evolution of the SO_2 plume heights observed by these different IR sensors is presented in Fig. 11c.

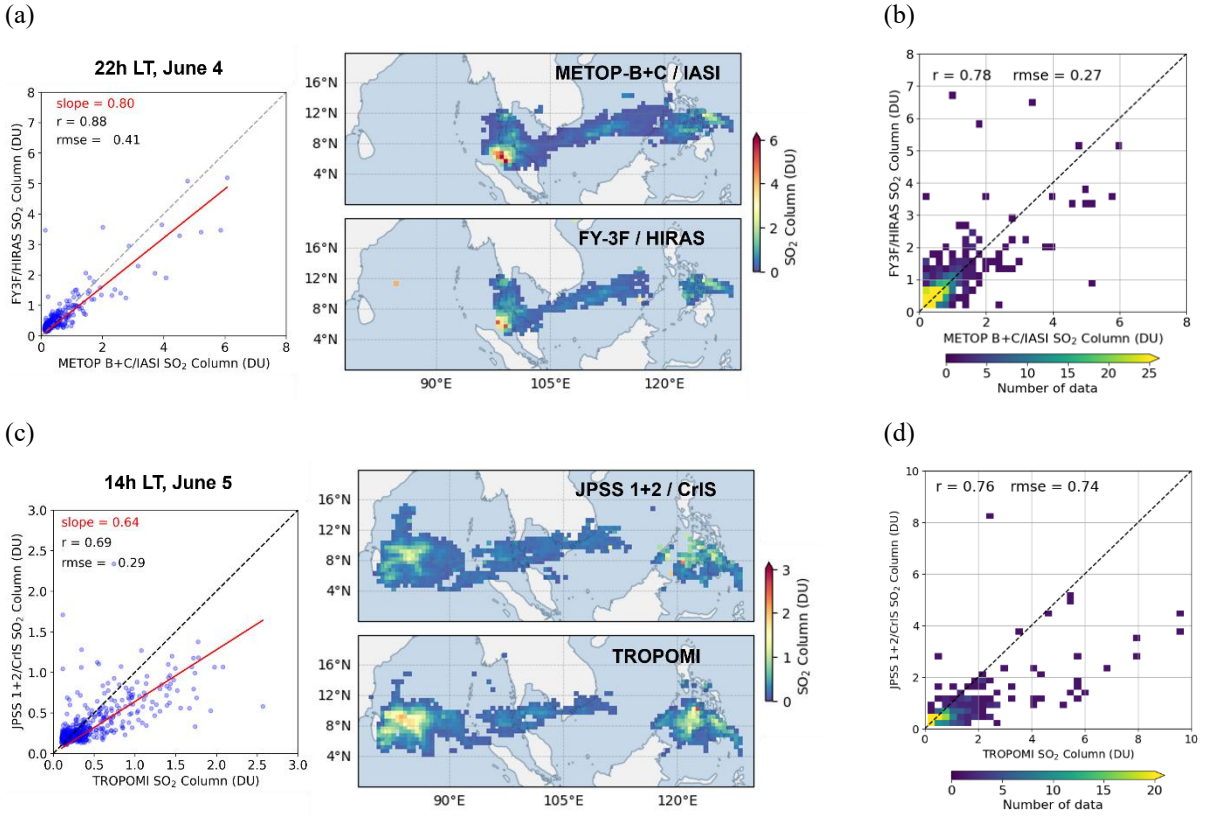

Figure 9: Validation of retrieval algorithms against independent satellite products. (a) Example of SO_2 total column comparison between Metop-B/C IASI and FY-3F/HIRAS at ~22 h LT on June 4, 2024. The datasets are resampled to 0.5° by 0.5° grids for point-to-point analysis; (b) Statistical validation using all spatiotemporally matched data points throughout the study period; (c) Similar to (a) but for the comparison between JPSS-1/2 CrIS and Sentinel-5P TROPOMI at ~14 h LT on June 5, 2024; (d) Same as (b) but for CrIS and TROPOMI.

All comparison datasets are resampled to 0.5° by 0.5° grids for point-to-point analysis. Fig. 9a illustrates a comparison instance between IASI and FY-3F/HIRAS at approximately 22h LT on June 4, 2024, with additional matched observation pairs provided in Figs. S18 and S19. To further evaluate the algorithm's performance, a statistical analysis was conducted by aggregating all matched data points throughout the study period (Fig. 9b). The results show a high correlation of 0.78 and an RMSE of 0.27 DU, demonstrating good consistency between HIRAS and the IASI products. The discrepancies observed at certain timestamps likely stem from non-synchronous overpasses (with time lags of several tens of minutes), which exert a more pronounced impact on such small-scale and rapidly evolving volcanic plumes. In addition, the spatial distributions of IASI SO_2 plume heights are provided in Figs. S20 and S21. Statistical assessment across the respective overpasses reveals that IASI heights are systematically higher than those from FY-3F/HIRAS, with mean values being 0.2–1.6 km higher and medians exhibiting a positive offset of 1–2 km. Such height discrepancies have been reported by Zeng et al. (2025). They are likely due

https://doi.org/10.5194/egusphere-2026-1745
Preprint. Discussion started: 16 April 2026

to the effects of inherent instrumental differences and distinct retrieval algorithms. The temporal evolution of the SO_2 plume heights observed by these different IR sensors is presented in Fig. 11c.

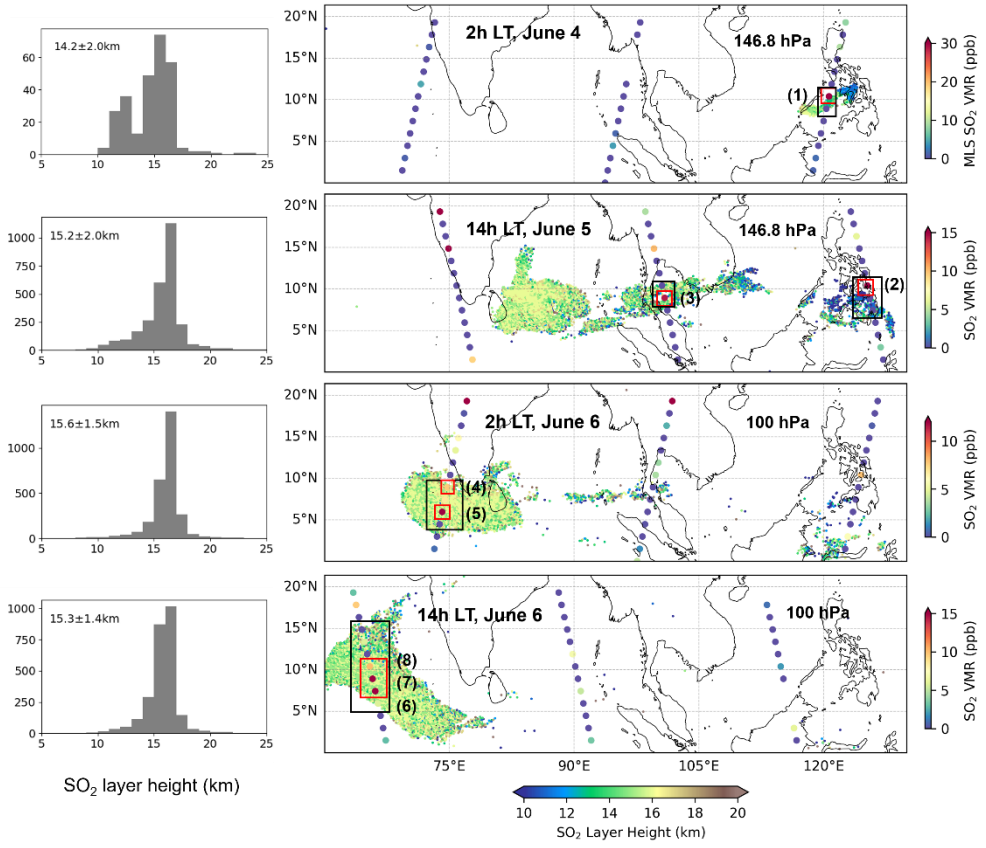

Figure 10: Validation of retrieved SO_2 plume layer heights using Aura/MLS limb sounding observations. The spatial maps overlay CrIS-retrieved heights with MLS SO_2 VMR at specific pressure levels (146.8 and 100 hPa). Histograms (left) quantify the CrIS height statistics for each scene. Black boxes indicate spatiotemporal collocation regions, while numbered red boxes (1–8) indicate footprints where detailed vertical profiles are analyzed in Figure S24.

Fig. 9c presents a comparison between TROPOMI and JPSS-1/2 CrIS at approximately 14h LT on June 5, with additional comparative results provided in Fig. S22. Throughout the study period, the SO_2 total columns from both sensors exhibit a correlation of 0.76 and an RMSE of 0.74 DU (Fig. 9d). Notably, TROPOMI retrievals tend to be higher than CrIS during the early eruptive stage, likely due to fundamental differences in their retrieval mechanisms. For IR sensors (CrIS), sensitivity to lower-tropospheric SO_2 strongly constrained by the thermal contrast and subject to strong water vapor interference, resulting in potential underestimation of SO_2 total column. Conversely, UV sensors (TROPOMI) rely on backscattered solar radiation to integrate the absorption signal across the entire atmospheric column, allowing them to maintain a lower detection threshold for low-altitude SO_2. Other sources of bias include differing plume height assumptions—TROPOMI assumes a fixed 15 km altitude, whereas CrIS utilizes retrieved heights ranging from 5 to 25 km—and discrepancies in observation time windows

https://doi.org/10.5194/egusphere-2026-1745
Preprint. Discussion started: 16 April 2026

(13h–14h LT for CrIS versus 12h–15h LT for TROPOMI, shown in Fig. S23), which introduces significant uncertainty when characterizing such a rapidly evolving plume.

5.4 Temporal evolution of SO_2 mass loading

The total SO_2 mass and its temporal evolution are quantified through the spatial integration of SO_2 column retrieved from multiple satellite sensors. All retrievals are resampled to uniform 0.5° by 0.5° grids prior to spatial integration to ensure consistency. To address inherent swath gaps of polar-orbiting satellites, a multi-satellite synergistic gap-filling strategy is implemented: Metop-B and -C IASI observations are merged into a unified composite, as are those from JPSS-1/2 CrIS observations. For FY-3F/HIRAS, the empty 0.5° grid cells within its swath gaps are directly filled using spatially coincident IASI data. FY-3E/HIRAS remains unfilled due to a lack of temporally coincident overpasses. Fig. S25 displays the SO_2 mass time series for individual IR sensors prior to gap-filling, revealing the significant uncertainties in single polar-orbiting estimates. Even for identical sensors on different platforms (e.g., the two CrIS instruments), SO_2 mass estimates vary substantially, particularly between 20 and 60 hours, which is primarily due to incomplete plume sampling caused by orbit geometries. The fused multi-satellite SO_2 mass time series (Fig. 11a) shows high consistency among IASI, CrIS, and FY-3F/HIRAS in capturing the mass evolution. The estimate from FY-3E/HIRAS is slightly lower due to the observation gaps.

GEO observations (GIIRS and GEMS) provide continuous, high-frequency monitoring of the SO_2 mass evolution during the initial eruptive phase (~20 h). FY-4B/GIIRS provides coverage from 1 to 15 hours post- eruption, particularly offering the first mass estimates. Notably, GIIRS estimates are systematically higher. This likely stems from its limited detection sensitivity: GIIRS only captures high-concentration SO_2 pixels while missing the lower ones. Thus, averaging only these high values within the 0.5° grids inflates the mean concentration, leading to an overestimation of the total integrated mass. GEMS observations, spanning 12 to 20 hours post-eruption, indicate that the SO_2 mass loading peaks during the daytime on June 4, although uncertainties remain (as discussed in Section 4.2.2). During this period, the high-frequency GEO observations provide indispensable support for tracking continuous mass evolution, which discrete LEO samplings could not fully capture.

Between 20 and 40 hours, a systematic bias is observed between UV (GEMS, TROPOMI) and IR (IASI, CrIS, HIRAS) mass estimates, with UV results being higher. This discrepancy is consistent with the cross-comparisons in Figs. 9 and S20, likely stemming from the superior sensitivity of UV instruments to lower-tropospheric SO_2. From June 5 onwards, as the western plume stabilizes at 14–16 km, the UV and IR mass estimate converge, due to comparable spectral sensitivities at these altitudes. The SO_2 mass time series reveals a continuous dilution and dispersion process following an exponential decay (Fig. 11b). Based on a combined fit of IASI, CrIS, and FY-3F/HIRAS data, the estimated e-folding time is 5.2 ± 0.5 days, which aligns well with the compilation of SO_2 lifetimes in volcanic plumes at a range of altitudes and latitudes reported by **Carn et al. (2016)**. Tracking is terminated once the total mass falls below 10 ktons, as detecting dilute plumes becomes increasingly challenging against background and instrument noise. This early cessation of tracking may result in a slight underestimation of the actual atmospheric SO_2 lifetime.

https://doi.org/10.5194/egusphere-2026-1745
Preprint. Discussion started: 16 April 2026

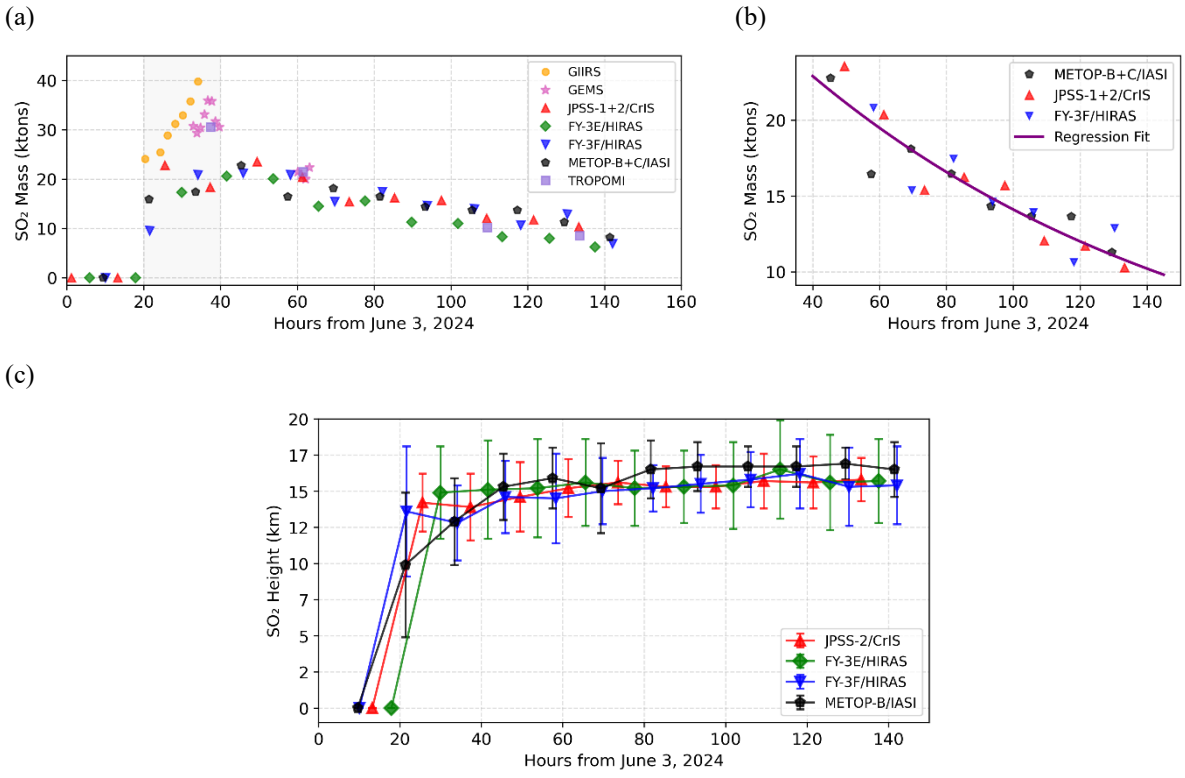

Figure 11: (a) Time series of volcanic SO_2 mass loading derived from multiple satellite sensors following the eruption, where the shaded gray region indicates the early monitoring phase covered by geostationary satellites. (b) Exponential decay fitting based on the fused IR observations (IASI, CrIS, FY-3F/HIRAS), yielding an estimated e-folding lifetime of 5.2 ± 0.5 days. (c) Time series of the mean SO_2 layer heights retrieved from the polar-orbiting IR sounders. Vertical error bars denote the standard deviations.

5.5 Comparative analysis of satellite observations and CAMS model simulations

This section compares the satellite-observed SO_2 results with the multi-level SO_2 products of Copernicus Atmosphere Monitoring Service (CAMS) forecasts to highlight the significance of the proposed high-resolution synergistic observation framework. The CAMS model is initialized twice daily (00:00 and 12:00 UTC), providing 5-day forecasts with a 3-hour temporal resolution, a 0.4° by 0.4° horizontal resolution, and 25 vertical layers (1000–1 hPa). Fig. S27 displays the CAMS SO_2 total columns from June 3, 12:00 UTC (~1 h post-eruption) to June 6. For simplicity, only the results for 00:00, 06:00, 12:00, and 18:00 UTC each day are shown in the figure. Fig. S28 plots the satellite observation results (CrIS and IASI) that are temporally close to the CAMS output times. All satellite observations are uniformly marked as UTC time corresponding to the sensor's overpass at the volcano location for comparison. Figure 12 presents a direct side-by-side comparison between the CAMS forecasts and the satellite observations for June 5, 2024.

Significant discrepancies between the model and satellite observations are identified in three areas: (1) Spatiotemporal evolution of the SO_2 plume. CAMS data fail to capture the critical first 13 hours post-eruption on June 3, with a massive plume appearing abruptly only at 00:00 UTC on June 4. In contrast, satellite observations provide a detailed record of the plume from

https://doi.org/10.5194/egusphere-2026-1745
Preprint. Discussion started: 16 April 2026

its generation to morphological evolution. Furthermore, while satellite observations reveal a rapid westward advection of the plume core, and the dissipation of the eastern plume near the crater by June 5, CAMS data simulate a significantly slower westward transport and suggest the persistence of the eastern plume near the source. (2) SO_2 total column density. Satellite observations record a rapid attenuation in SO_2 loading, reaching ~1 DU by June 6. CAMS data, however, systematically overestimate the concentrations, maintaining values as high as 4–5 DU during the same period. (3) SO_2 vertical distribution. Vertical profile analysis (Fig. S29) shows that CAMS SO_2 data are mainly distributed in the height range of approximately 800 to 300 hPa **(Inness et al., 2022)**. This is quite different from the satellite retrievals, especially in the later stage, the height of the plume body being concentrated at 100–200 hPa (~15–16 km).

These results indicate that global models like CAMS face limitations in capturing initial emissions, determining precise injection heights, and predicting transport trajectories for small-scale volcanic eruptions. These findings underscore the indispensable role of high-resolution synergistic satellite observation frameworks in the accurate monitoring and validation of rapidly evolving atmospheric events.

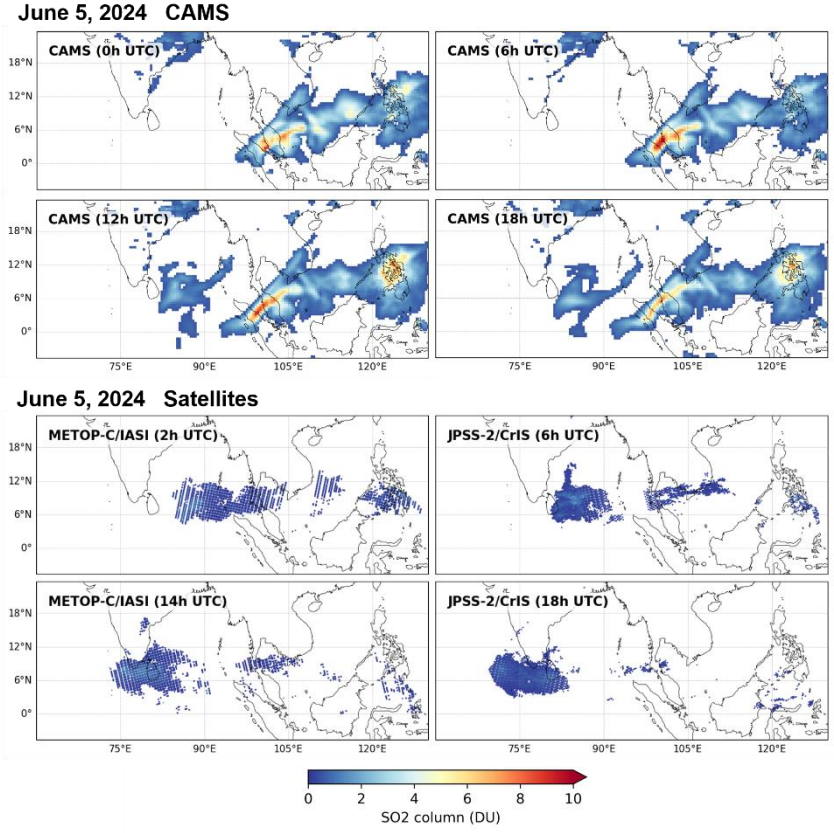

Figure 12: Direct comparison of SO_2 spatial distribution between CAMS forecasts (top) and spatiotemporally matched satellite observations (bottom) on June 5, 2024. The satellite overpass times (UTC at the volcano) are paired with the closest 6-hourly CAMS outputs to highlight discrepancies in transport speed and plume morphology.

https://doi.org/10.5194/egusphere-2026-1745
Preprint. Discussion started: 16 April 2026

6. Conclusions

This study constructs a synergistic multi-satellite observation framework by developing a dedicated FY-4B/GIIRS geostationary infrared hyperspectral SO_2 retrieval algorithm and integrating data from both GEO (GIIRS, GEMS) and LEO (HIRAS, CrIS, IASI, TROPOMI, and MLS). Taking the June 2024 eruption of Mt. Kanlaon in the Philippines as a case study, the framework achieves high-spatiotemporal-resolution three-dimensional monitoring of the SO_2 plume throughout its entire lifecycle, from the initial eruption (approximately 1 hour post-event) to long-range transport (persisting for over 5 days).

Our findings indicate that: (1) GEO observations provide high-temporal-resolution data. FY-4B/GIIRS captures the earliest quantitative SO_2 observations and the nighttime evolution of the plume, while GEMS records critical details of the SO_2 mass loading peak and evolution during the daytime, revealing rapid dynamics. (2) The LEO constellation effectively extends the spatiotemporal coverage. LEO sensors provide continuous tracking after the plume moves beyond the fixed field of view of GEO satellites, yielding a complete evolutionary record. The estimated SO_2 e-folding time based on fused LEO data is 5.2 ± 0.5 days, providing a quantitative basis for understanding the atmospheric lifetime of volcanic emissions. (3) Multi-platform synergy enables cross-validation and integrated analysis. The consistency in SO_2 total columns across sensors (e.g., HIRAS and CrIS), combined with independent plume height validation from MLS, ensure the reliability of the results. The multi-observation analysis reveals evolutionary details: the western plume rapidly ascends and stabilizes at 14-16 km while moving westward, whereas the eastern plume dissipates quickly at lower altitudes of 5-12 km. This synergistic approach compensates for the limitations of individual sensors in spatial coverage or vertical resolution. (4) Comparisons with atmospheric chemical model outputs highlight the value of high-resolution observations. Significant discrepancies between our observations and CAMS model simulations are identified in terms of spatial distribution, concentration, and vertical structure. These biases suggest that current global models still struggle to represent small-to-medium scale volcanic eruptions, underscoring the role of this framework in constraining and improving model schemes.

With the continued deployment of geostationary hyperspectral sounders such as IRS on the European MTG satellite, GIIRS on FY-4B/C and subsequent Fengyun satellites, the synergistic framework develops in this study can be directly applied to monitoring volcanic activity worldwide. Since these emerging sensors only cover the ν1 weak SO_2 absorption band, our retrieval algorithm possesses high universality and can be readily adapted across platforms. Future research will therefore focus on extending this methodology to establish a coordinated global observation network. Ultimately, integrating global geostationary resources will lead to a comprehensive volcanic monitoring network, providing unprecedented support for volcanology, disaster prevention, and climate assessment.

https://doi.org/10.5194/egusphere-2026-1745
Preprint. Discussion started: 16 April 2026

Data availability

The FY-4B/GIIRS and FY-3/HIRAS Level 1 data are publicly available from the FengYun Satellite Data Center (https://data.nsmc.org.cn/DataPortal/en/home/index.html); the JPSS-1/2 CrIS Level 1B data and MLS Level 2 SO_2 data are available at GES DISC (https://search.earthdata.nasa.gov/); the IASI Level2 SO_2 data are available from the IASI Portal (https://iasi.aeris-data.fr/); the GEMS data are available from the National Environmental Satellite8/ Center (https://nesc.nier.go.kr/en/html/index.do); the TROPOMI SO_2 data can be downloaded from the S5P-PAL Data Portal (https://data-portal.s5p-pal.com/products/so2cbr.html). The CAMS SO_2 data are available from ECMWF (https://www.ecmwf.int/en/forecasts/dataset/cams-global-atmospheric-composition-forecasts).

Author contributions

Shangyi Liu: Methodology, Software, Validation, Formal analysis, Writing– original draft, Writing– review & editing. **Yingjun Zheng:** Writing– review & editing. **Mengya Sheng:** Writing– review & editing. **Lu Lee:** Resources, data curation, Writing– review & editing. **Chengli Qi:** Resources, data curation, Writing– review & editing. **Feng Lu:** Resources, data curation, Writing– review & editing. **Bruno Franco:** Resources, data curation, Writing- Reviewing and Editing. **Lieven Clarisse:** Resources, data curation, Writing- Reviewing and Editing. **Cathy Clerbaux:** Resources, data curation, Writing-Reviewing and Editing. **Nicolas Theys:** Resources, data curation, Writing- Reviewing and Editing. **Jhoon Kim:** Resources, data curation, Writing- Reviewing and Editing. **Zhao-Cheng Zeng:** Conceptualization, Methodology, Software, Supervision, Writing– review & editing, Funding acquisition

Competing interests

The contact author has declared that none of the authors has any competing interests.

Disclaimer

Publisher's note: Copernicus Publications remains neutral with regard to jurisdictional claims made in the text, published maps, institutional affiliations, or any other geographical representation in this paper. While Copernicus Publications makes every effort to include appropriate place names, the final responsibility lies with the authors.

Acknowledgements

Z.-C. Zeng acknowledges financial support of the National Satellite Meteorological Center (NSMC) of the China Meteorological Administration (CMA). The research has been supported by the HIRS Prodex arrangement (ESA-BELSPO).

https://doi.org/10.5194/egusphere-2026-1745
Preprint. Discussion started: 16 April 2026

L. Clarisse is Senior Research Associate supported by the Belgian F.R.S.-FNRS. N. Theys acknowledges financial support from ESA S5P PAL, ESA S5P ATM-MPC and Belgium Prodex TRACE-S5P projects. We also thank the GEMS science team for their L2 product.

Financial support

This study was supported by the National Natural Science Foundation of China (No. 42275142) and the National Key R&D Program of China (No. 2022YFA1003800).

References

Ackerman, S. A., Schreiner, A. J., Schmit, T. J., Woolf, H. M., Li, J., and Pavolonis, M.: Using the GOES Sounder to monitor upper level SO2 from volcanic eruptions, Journal of Geophysical Research: Atmospheres, 113, D14, https://doi.org/10.1029/2007JD009622, 2008.

Carboni, E., Grainger, R., Walker, J., Dudhia, A., and Siddans, R.: A new scheme for sulphur dioxide retrieval from IASI measurements: Application to the Eyjafjallajökull eruption of April and May 2010, Atmospheric Chemistry and Physics, 12, 11417–11434, https://doi.org/10.5194/acp-12-11417-2012, 2012.

Carn, S. A., Strow, L. L., De Souza–Machado, S., Edmonds, Y., and Hannon, S.: Quantifying tropospheric volcanic emissions with AIRS: The 2002 eruption of Mt. Etna (Italy), Geophysical Research Letters, 32, 2004GL021034, https://doi.org/10.1029/2004GL021034, 2005.

Carn, S. A., Clarisse, L., and Prata, A. J.: Multi-decadal satellite measurements of global volcanic degassing, Journal of Volcanology and Geothermal Research, 311, 99–134, https://doi.org/10.1016/j.jvolgeores.2016.01.002, 2016.

Clarisse, L., Coheur, P. F., Prata, A. J., Hurtmans, D., Razavi, A., Phulpin, T., Hadji-Lazaro, J., and Clerbaux, C.: Tracking and quantifying volcanic SO2 with IASI, the September 2007 eruption at Jebel at Tair, Atmospheric Chemistry and Physics, 8, 7723–7734, https://doi.org/10.5194/acp-8-7723-2008, 2008.

Clarisse, L., Coheur, P.-F., Theys, N., Hurtmans, D., and Clerbaux, C.: The 2011 Nabro eruption, a SO2 plume height analysis using IASI measurements, Atmospheric Chemistry and Physics, 14, 3095–3111, https://doi.org/10.5194/acp-14-3095-2014, 2014.

Clarisse, L., Franco, B., Fabris, L., Theys, N., Hadji-Lazaro, J., Hurtmans, D., Clerbaux, C., and Coheur, P.-F.: An 18-year record of atmospheric sulphur dioxide (SO2) derived from IASI measurements, submitted to Earth System Science Data, submitted, 2026.

Clarisse, L. and Prata, F.: Infrared sounding of volcanic ash, in: Volcanic Ash, Elsevier, 189–215, https://doi.org/10.1016/B978-0-08-100405-0.00017-3, 2016.

https://doi.org/10.5194/egusphere-2026-1745
Preprint. Discussion started: 16 April 2026

Clerbaux, C., Boynard, A., Clarisse, L., George, M., Hadji-Lazaro, J., Herbin, H., Hurtmans, D., Pommier, M., Razavi, A., Turquety, S., Wespes, C., and Coheur, P.-F.: Monitoring of atmospheric composition using the thermal infrared IASI/MetOp sounder, Atmospheric Chemistry and Physics, 9, 6041–6054, https://doi.org/10.5194/acp-9-6041-2009, 2009.

Clerbaux, C., Coheur, P.-F., Clarisse, L., Hadji-Lazaro, J., Hurtmans, D., Turquety, S., Bowman, K., Worden, H., and Carn, S. A.: Measurements of SO2 profiles in volcanic plumes from the NASA Tropospheric Emission Spectrometer (TES), Geophysical Research Letters, 35, L22807, https://doi.org/10.1029/2008GL035566, 2008.

Corradini, S., Merucci, L., and Prata, A. J.: Retrieval of SO2 from thermal infrared satellite measurements: Correction procedures for the effects of volcanic ash, Atmospheric Measurement Techniques, 2, 177–191, https://doi.org/10.5194/amt-2-177-2009, 2009.

Eisinger, M. and Burrows, J. P.: Tropospheric sulfur dioxide observed by the ERS–2 GOME instrument, Geophysical Research Letters, 25, 4177–4180, https://doi.org/10.1029/1998GL900128, 1998.

EUMETSAT: MTG-S IRS Science Plan, Doc. No. EUM2033485, available at: https://user.eumetsat.int/s3/ope-eup-strapi-media/MTG_S_IRS_Science_Plan_47145497b0.pdf, 2025.

Global Volcanism Program: Report on Kanlaon (Philippines), Weekly Volcanic Activity Report, 29 May–4 June 2024, edited by: Sennert, S., Smithsonian Institution and US Geological Survey, 2024.

Han, Y., Revercomb, H., Cromp, M., Gu, D., Johnson, D., Mooney, D., Scott, D., Strow, L., Bingham, G., Borg, L., Chen, Y., DeSlover, D., Esplin, M., Hagan, D., Jin, X., Knuteson, R., Motteler, H., Predina, J., Suwinski, L., and Zavyalov, V.: Suomi NPP CrIS measurements, sensor data record algorithm, calibration and validation activities, and record data quality, Journal of Geophysical Research: Atmospheres, 118, 12734–12748, https://doi.org/10.1002/2013JD020344, 2013.

Hyman, D. M. and Pavolonis, M. J.: Probabilistic retrieval of volcanic SO2 layer height and partial column density using the Cross-track Infrared Sounder (CrIS), Atmospheric Measurement Techniques, 13, 5891–5921, https://doi.org/10.5194/amt-13-5891-2020, 2020.

Inness, A., Ades, M., Balis, D., Efremenko, D., Flemming, J., Hedelt, P., Koukouli, M.-E., Loyola, D., and Ribas, R.: Evaluating the assimilation of S5P/TROPOMI near real-time SO2 columns and layer height data into the CAMS integrated forecasting system (CY47R1), based on a case study of the 2019 Raikoke eruption, Geoscientific Model Development, 15, 971–994, https://doi.org/10.5194/gmd-15-971-2022, 2022.

Kim, J., Jeong, U., Ahn, M.-H., Kim, J. H., Park, R. J., Lee, H., Song, C. H., Choi, Y.-S., Lee, K.-H., Yoo, J.-M., Jeong, M.-J., Park, S. K., Lee, K.-M., Song, C.-K., Kim, S.-W., Kim, Y. J., Kim, S.-W., Kim, M., Go, S., and Choi, Y.: New era of air quality monitoring from space: Geostationary Environment Monitoring Spectrometer (GEMS), Bulletin of the American Meteorological Society, 101, E1–E22, https://doi.org/10.1175/BAMS-D-18-0013.1, 2020.

Krotkov, N. A., Carn, S. A., Krueger, A. J., Bhartia, P. K., and Yang, K.: Band residual difference algorithm for retrieval of SO2 from the aura Ozone Monitoring Instrument (OMI), IEEE Transactions on Geoscience and Remote Sensing, 44, 1259–1266, https://doi.org/10.1109/TGRS.2005.861932, 2006.

https://doi.org/10.5194/egusphere-2026-1745
Preprint. Discussion started: 16 April 2026

Krueger, A. J.: Sighting of El Chichón Sulfur dioxide clouds with the Nimbus 7 total ozone mapping spectrometer, Science, 220, 1377–1379, https://doi.org/10.1126/science.220.4604.1377, 1983.

Kuhn, H. W.: The Hungarian method for the assignment problem, Naval Research Logistics, 2, 83–97, https://doi.org/10.1002/nav.3800020109, 1955.

Lee, C., Richter, A., Weber, M., and Burrows, J. P.: SO2 retrieval from SCIAMACHY using the weighting function DOAS (WFDOAS) technique: comparison with standard DOAS retrieval, Atmospheric Chemistry and Physics, 8, 6137–6145, https://doi.org/10.5194/acp-8-6137-2008, 2008.

Lee, H., Park, J., and Yang, J.: Geostationary Environment Monitoring Spectrometer (GEMS) algorithm theoretical basis document: SO2 retrieval algorithm (Issue 1.3), National Institute of Environmental Research (NIER), Republic of Korea, 2024.

Li, C., Krotkov, N. A., Joiner, J., Carn, S., Fioletov, V., McLinden, C., Griffin, D., Liu, X., and Chong, H.: Hourly sulfur dioxide observations over north America: first retrieval results from TEMPO, Geophysical Research Letters, 52, e2025GL115788, https://doi.org/10.1029/2025GL115788, 2025.

Li, J., Menzel, W. P., Schmit, T. J., and Schmetz, J.: Applications of geostationary hyperspectral infrared sounder observations: progress, challenges, and future perspectives, Bulletin of the American Meteorological Society, 103, E2733–E2755, https://doi.org/10.1175/BAMS-D-21-0328.1, 2022a.

Li, L., Ni, Z., Qi, C., Yang, L., and Han, C.: Pre–launch radiometric calibration of geostationary interferometric infrared sounder on FengYun–4B satellite, Acta Optica Sinica, 42, 0630001, https://doi.org/10.3788/AOS202242.0630001, 2022b.

Li, X., Zhu, L., Sun, H., Li, J., Lv, X., Qi, C., and Yan, H.: A channel selection methodology for enhancing volcanic SO2 monitoring using FY-3E/HIRAS-II hyperspectral data, Atmospheric Measurement Techniques, 18, 2333–2352, https://doi.org/10.5194/amt-18-2333-2025, 2025.

Liu, S., Hua, J., Wang, H., Han, S., Lee, L., Qi, C., Lu, F., Luo, Y., Zhao, X., Li, Z., Kim, S., Song, C. K., Kanaya, Y., Keppens, A., Lambert, J., Clerbaux, C., and Zeng, Z.: Observing the diurnal variation of atmospheric ozone from the Geostationary Interferometric Infrared Sounder (GIIRS) over east asia, Journal of Geophysical Research: Atmospheres, 130, e2024JD042292, https://doi.org/10.1029/2024JD042292, 2025.

Livesey, N. J., Read, W. G., Wagner, P. A., Froidevaux, L., Santee, M. L., Schwartz, M. J., and Lay, R. R.: Earth Observing System (EOS) Aura Microwave Limb Sounder (MLS) version 5.0x level 2 and 3 data quality and description document, Jet Propulsion Laboratory, available at: https://mls.jpl.nasa.gov/data/v5-0_data_quality_document.pdf, 2022.

Mills, M. J., Schmidt, A., Easter, R., Solomon, S., Kinnison, D. E., Ghan, S. J., Neely, R. R., Marsh, D. R., Conley, A., Bardeen, C. G., and Gettelman, A.: Global volcanic aerosol properties derived from emissions, 1990–2014, using CESM1(WACCM), Journal of Geophysical Research: Atmospheres, 121, 2332–2348, https://doi.org/10.1002/2015JD024290, 2016.

Park, J., Lee, H., Yang, J., Hong, H., Kim, J., Roozendael, M. V., Theys, N., Li, C., Ahn, M.-H., Lee, D., Park, J., Choi, W., Park, R., and Kim, D.: The hourly volcanic SO2 column density and physical characteristics using Geostationary Environment Monitoring Spectrometer (GEMS) measurements, EGU General Assembly 2023, Vienna, Austria, 24–28 Apr 2023, EGU23-10841, https://doi.org/10.5194/egusphere-egu23-10841, 2023..

https://doi.org/10.5194/egusphere-2026-1745
Preprint. Discussion started: 16 April 2026

Prata, A. J.: Satellite detection of hazardous volcanic clouds and the risk to global air traffic, Natural Hazards, 51, 303–324, https://doi.org/10.1007/s11069-008-9273-z, 2009.

Prata, A. J. and Kerkmann, J.: Simultaneous retrieval of volcanic ash and SO2 using MSG–SEVIRI measurements, Geophysical Research Letters, 34, L05801, https://doi.org/10.1029/2006GL028691, 2007.

Pumphrey, H. C., Read, W. G., Livesey, N. J., and Yang, K.: Observations of volcanic SO2 from MLS on Aura, Atmospheric Measurement Techniques, 8, 195–209, https://doi.org/10.5194/amt-8-195-2015, 2015.

Queißer, M., Burton, M., Theys, N., Pardini, F., Salerno, G., Caltabiano, T., Varnam, M., Esse, B., and Kazahaya, R.: TROPOMI enables high resolution SO2 flux observations from Mt. Etna, Italy, and beyond, Scientific Reports, 9, 957, https://doi.org/10.1038/s41598-018-37807-w, 2019.

Rix, M., Valks, P., Hao, N., Loyola, D., Schlager, H., Huntrieser, H., Flemming, J., Koehler, U., Schumann, U., and Inness, A.: Volcanic SO2, BrO and plume height estimations using GOME–2 satellite measurements during the eruption of Eyjafjallajökull in May 2010, Journal of Geophysical Research: Atmospheres, 117, D20, https://doi.org/10.1029/2011JD016718, 2012.

Robock, A.: Volcanic eruptions and climate, Reviews of Geophysics, 38, 191–219, https://doi.org/10.1029/1998RG000054, 2000.

Rodgers, C. D.: Inverse Methods for Atmospheric Sounding: Theory and Practice, vol. 2, World Scientific, https://doi.org/10.1142/3171, 2000.

Schmidt, A., Mills, M. J., Ghan, S., Gregory, J. M., Allan, R. P., Andrews, T., Bardeen, C. G., Conley, A., Forster, P. M., Gettelman, A., Portmann, R. W., Solomon, S., and Toon, O. B.: Volcanic radiative forcing from 1979 to 2015, Journal of Geophysical Research: Atmospheres, 123, 12491–12508, https://doi.org/10.1029/2018JD028776, 2018.

Schmidt, A., Ostro, B., Carslaw, K. S., Wilson, M., Thordarson, T., Mann, G. W., and Simmons, A. J.: Excess mortality in Europe following a future Laki-style Icelandic eruption, Proceedings of the National Academy of Sciences of the United States of America, 108, 15710–15715, https://doi.org/10.1073/pnas.1108569108, 2011.

Theys, N., De Smedt, I., Van Gent, J., Danckaert, T., Wang, T., Hendrick, F., Stavrakou, T., Bauduin, S., Clarisse, L., Li, C., Krotkov, N., Yu, H., Brenot, H., and Van Roozendael, M.: Sulfur dioxide vertical column DOAS retrievals from the Ozone Monitoring Instrument: Global observations and comparison to ground–based and satellite data, Journal of Geophysical Research: Atmospheres, 120, 2470–2491, https://doi.org/10.1002/2014JD022657, 2015.

Theys, N., De Smedt, I., Yu, H., Danckaert, T., Van Gent, J., Hörmann, C., Wagner, T., Hedelt, P., Bauer, H., Romahn, F., Pedergnana, M., Loyola, D., and Van Roozendael, M.: Sulfur dioxide retrievals from TROPOMI onboard Sentinel-5 Precursor: Algorithm theoretical basis, Atmospheric Measurement Techniques, 10, 119–153, https://doi.org/10.5194/amt-10-119-2017, 2017.

Theys, N., Fioletov, V., Li, C., De Smedt, I., Lerot, C., McLinden, C., Krotkov, N., Griffin, D., Clarisse, L., Hedelt, P., Loyola, D., Wagner, T., Kumar, V., Inness, A., Ribas, R., Hendrick, F., Vlietinck, J., Brenot, H., and Van Roozendael, M.: A sulfur

https://doi.org/10.5194/egusphere-2026-1745
Preprint. Discussion started: 16 April 2026

dioxide Covariance-Based Retrieval Algorithm (COBRA): Application to TROPOMI reveals new emission sources, Atmospheric Chemistry and Physics, 21, 16727–16744, https://doi.org/10.5194/acp-21-16727-2021, 2021.

Timmreck, C.: Modeling the climatic effects of large explosive volcanic eruptions, WIREs Climate Change, 3, 545–564, https://doi.org/10.1002/wcc.192, 2012.

Urai, M.: Sulfur dioxide flux estimation from volcanoes using Advanced Spaceborne Thermal Emission and Reflection Radiometer—A case study of Miyakejima volcano, Japan, Journal of Volcanology and Geothermal Research, 134, 1–13, https://doi.org/10.1016/j.jvolgeores.2003.11.008, 2004.

Veefkind, J. P., Aben, I., McMullan, K., Förster, H., De Vries, J., Otter, G., Claas, J., Eskes, H. J., De Haan, J. F., Kleipool, Q., Van Weele, M., Hasekamp, O., Hoogeveen, R., Landgraf, J., Snel, R., Tol, P., Ingmann, P., Voors, R., Kruizinga, B., and Levelt, P. F.: TROPOMI on the ESA Sentinel-5 Precursor: A GMES mission for global observations of the atmospheric composition for climate, air quality and ozone layer applications, Remote Sensing of Environment, 120, 70–83, https://doi.org/10.1016/j.rse.2011.09.027, 2012.

Von Clarmann, T., Grabowski, U., and Kiefer, M.: On the role of non-random errors in inverse problems in radiative transfer and other applications, Journal of Quantitative Spectroscopy and Radiative Transfer, 71, 39–46, https://doi.org/10.1016/S0022-4073(01)00010-3, 2001.

Walker, J. C., Carboni, E., Dudhia, A., and Grainger, R. G.: Improved detection of sulphur dioxide in volcanic plumes using satellite-based hyperspectral infrared measurements: Application to the Eyjafjallajökull 2010 eruption, Journal of Geophysical Research: Atmospheres, 117, D20, https://doi.org/10.1029/2011JD016810, 2012.

Walker, J. C., Dudhia, A., and Carboni, E.: An effective method for the detection of trace species demonstrated using the MetOp Infrared Atmospheric Sounding Interferometer, Atmospheric Measurement Techniques, 4, 1567–1580, https://doi.org/10.5194/amt-4-1567-2011, 2011.

Wang, G., Zhang, R., Gomez, M. E., Yang, L., Levy Zamora, M., Hu, M., Lin, Y., Peng, J., Guo, S., Meng, J., Li, J., Cheng, C., Hu, T., Ren, Y., Wang, Y., Gao, J., Cao, J., An, Z., Zhou, W., and Molina, M. J.: Persistent sulfate formation from London fog to Chinese haze, Proceedings of the National Academy of Sciences of the United States of America, 113, 13630–13635, https://doi.org/10.1073/pnas.1616540113, 2016.

Waters, J. W., Froidevaux, L., Harwood, R. S., Jarnot, R. F., Pickett, H. M., Read, W. G., Siegel, P. H., Cofield, R. E., Filipiak, M. J., Flower, D. A., Holden, J. R., Lau, G. K., Livesey, N. J., Manney, G. L., Pumphrey, H. C., Santee, M. L., Wu, D. L., Cuddy, D. T., Lay, R. R., and Walch, M. J.: The Earth Observing System Microwave Limb Sounder (EOS MLS) on the aura Satellite, IEEE Transactions on Geoscience and Remote Sensing, 44, 1075–1092, https://doi.org/10.1109/TGRS.2006.873771, 2006.

Yang, K., Dickerson, R. R., Carn, S. A., Ge, C., and Wang, J.: First observations of SO2 from the satellite Suomi NPP OMPS: Widespread air pollution events over China, Geophysical Research Letters, 40, 4957–4962, https://doi.org/10.1002/grl.50952, 2013.

https://doi.org/10.5194/egusphere-2026-1745
Preprint. Discussion started: 16 April 2026

Zeng, Z.-C.: Global carbon monoxide retrieval from the hyperspectral infrared atmospheric sounder-II onboard FengYun-3E in a dawn-dusk sun-synchronous orbit, Journal of Quantitative Spectroscopy and Radiative Transfer, 333, 109336, https://doi.org/10.1016/j.jqsrt.2024.109336, 2025.

Zeng, Z.-C., Clarisse, L., Franco, B., Clerbaux, C., Theys, N., Qi, C., Lee, L., Zhu, L., Hu, X., Gu, M., and Zhang, P.: Volcanic sulfur dioxide monitored from a constellation of FengYun hyperspectral infrared sounders in dawn-dusk, mid-morning, and afternoon sun-synchronous orbits, Remote Sensing of Environment, 331, 115057, https://doi.org/10.1016/j.rse.2025.115057, 2025.

Zeng, Z.-C., Franco, B., Clarisse, L., Lee, L., Qi, C., and Lu, F.: Observing a volatile organic compound from a geostationary infrared sounder: HCOOH from FengYun-4B/GIIRS, Journal of Geophysical Research: Atmospheres, 129, e2024JD041352, https://doi.org/10.1029/2024JD041352, 2024.

Zeng, Z.-C., Lee, L., and Qi, C.: Diurnal carbon monoxide observed from a geostationary infrared hyperspectral sounder: First result from GIIRS on board FengYun-4B, Atmospheric Measurement Techniques, 16, 3059–3083, https://doi.org/10.5194/amt-16-3059-2023, 2023a.

Zeng, Z.-C., Lee, L., Qi, C., Clarisse, L., and Van Damme, M.: Optimal estimation retrieval of tropospheric ammonia from the Geostationary Interferometric Infrared Sounder on board FengYun-4B, Atmospheric Measurement Techniques, 16, 3693–3713, https://doi.org/10.5194/amt-16-3693-2023, 2023b.

Zhang, P., Hu, X., Lu, Q., Zhu, A., Lin, M., Sun, L., Chen, L., and Xu, N.: FY-3E: The first operational meteorological satellite mission in an early morning orbit, Advances in Atmospheric Sciences, 39, 1–8, https://doi.org/10.1007/s00376-021-1304-7, 2022.